

NASA Contractor Report 198494  
R95-5.101.0003-3

# A Three-Dimensional Linearized Unsteady Euler Analysis for Turbomachinery Blade Rows

Matthew D. Montgomery and Joseph M. Verdon  
*United Technologies Research Center  
East Hartford, Connecticut*

June 1996

Prepared for  
Lewis Research Center  
Under Contract NAS3-25425



National Aeronautics and  
Space Administration



# A Three-Dimensional Linearized Unsteady Euler Analysis for Turbomachinery Blade Rows

## Contents

Summary	1
1 Introduction	2
2 Unsteady Flow through a Blade Row	4
3 Nonlinear Aerodynamic Equations	6
4 Linearized Unsteady Aerodynamic Model	8
5 Numerical Model for the Linearized Equations	11
5.1 Finite Volume Equations . . . . .	11
5.2 Evaluation of Flux Terms . . . . .	13
5.3 Pseudo-Time Integration . . . . .	16
6 Numerical Results	18
6.1 Flat-Plate Stator . . . . .	20
6.2 3D Tenth Standard Configuration . . . . .	21
7 Concluding Remarks	29
References	30



# **A Three-Dimensional Linearized Unsteady Euler Analysis for Turbomachinery Blade Rows**

## **Summary**

A three-dimensional, linearized, Euler analysis is being developed to provide an efficient unsteady aerodynamic analysis that can be used to predict the aeroelastic and aeroacoustic response characteristics of axial-flow turbomachinery blading. The field equations and boundary conditions needed to describe nonlinear and linearized inviscid unsteady flows through a blade row operating within a cylindrical annular duct are presented in this report. In addition, a numerical model for linearized inviscid unsteady flow, which is based upon an existing nonlinear, implicit, wave-split, finite volume analysis, is described. The linearized aerodynamic and numerical models have been implemented into an unsteady flow code, called LINFLUX. A preliminary version of the LINFLUX code is applied herein to selected, benchmark, three-dimensional, subsonic, unsteady flows, to illustrate its current capabilities and to uncover existing problems and deficiencies. The numerical results indicate that good progress has been made toward the development of a reliable and useful three-dimensional prediction capability. However, some problems, associated with the implementation of an unsteady displacement field and numerical errors near solid boundaries, still exist. Also, accurate far-field conditions must be incorporated into the LINFLUX analysis, so that this analysis can be applied to unsteady flows driven by arbitrary external aerodynamic excitations. These issues will be addressed in our future work.

# 1. Introduction

The development of analyses to predict unsteady flows in axial-flow turbomachines is motivated primarily by the need to predict the aeroelastic (flutter and forced vibration) and aeroacoustic (sound generation, transmission and reflection) characteristics of the blading. Accurate and efficient aerodynamic analyses are needed to determine the unsteady loads that act on the blades and the unsteady pressure responses that persist upstream and downstream of the blade row, for various sources of excitation. These excitations include structural (blade) motions and aerodynamic disturbances at inlet and exit that carry energy towards the blade row. The computational resources required to simulate nonlinear and viscous unsteady fluid dynamic behavior continues to prohibit the use of such simulations in detailed aeroelastic or aeroacoustic design studies. Therefore, approximate, e.g., linearized inviscid, analyses are needed to provide efficient predictions of unsteady aerodynamic response phenomena.

Until recently, the linearized analyses available for turbomachinery aeroelastic and aeroacoustic applications, have been based on two- and three-dimensional, classical methods [Whi87, Nam87]. Such methods are very efficient, but are restricted to shock-free flows through lightly-loaded blade rows. Because of these limitations, unsteady aerodynamic linearizations relative to nonuniform potential mean flows have been developed [Ver93]. Such analyses account for the effects of real blade geometry, mean blade loading, and operation at transonic Mach numbers. They have received considerable attention in recent years and are now being applied in aeroelastic and aeroacoustic design studies. However, more comprehensive linearizations are needed to predict three-dimensional unsteady flows in which the effects of radial velocity and mean swirl are important, and two- and three-dimensional flows in which strong shocks occur. For such flows, the nonlinear Euler equations are required to model the nonisentropic and rotational mean or steady background flow and linearized versions of these equations are required to model the unsteady perturbations.

Thus, much attention is now being given to the development of two- [HC93a, HC93b, KK93, MV95] and three-dimensional [HL92, HCL93] linearized Euler analyses. As in the earlier linearizations with respect to potential mean flows, the linearized Euler equations are developed in the frequency domain for temporally and circumferentially periodic unsteady excitations, both to remove physical time-dependence from the resulting linear problem and to limit the computational domain to a single extended blade passage region. Unlike the earlier linearizations, the linearized Euler equations are solved over a deforming solution domain [HC93a, Gil93] so that troublesome extrapolation terms in the blade surface conditions can be replaced with more tractable source terms in the linearized unsteady field equations. Also, shock and wake effects are “captured”, within a conservative discrete formulation, rather than “fitted” by imposing shock and wake jump conditions. Finally, because of the large number of unknowns involved, the discretized linear unsteady equations are solved iteratively, rather than by direct matrix inversion.

Under the present effort, we have proceeded with the development of a three-dimensional linearized Euler analysis, which is based on a modern, implicit, flux-split, finite-volume, numerical model. The three-dimensional unsteady aerodynamic and numerical models have been formulated in the frequency-domain and implemented into a computer code, called

LINFLUX. The numerical model and the LINFLUX code are based on the high-resolution, wave-split, finite-volume scheme developed by Whitfield, Janus and Simpson [WJS88] for nonlinear unsteady flows, and implemented into the turbomachinery analysis, TURBO, by Janus, Horstman and Whitfield [JHW92]. The wave or flux splitting allows a sharp resolution of nonlinear shock phenomena—a feature which could facilitate the accurate prediction of impulsive shock loads with the linearized analysis in the future.

A two-dimensional version of the LINFLUX analysis has been reported in [MV95, VMK95], where numerical results for unsteady flows excited by prescribed blade motions and external aerodynamic disturbances are provided and compared with those of the linearized potential analysis, LINFLO [Ver93] and the nonlinear Euler/Navier-Stokes analysis, NPHASE [HSR91, SLH<sup>+</sup>94, AV94]. NPHASE is a two-dimensional counterpart of the TURBO analysis. These comparisons indicate that the 2D LINFLUX analysis gives accurate response information for unsteady subsonic flows excited by blade vibrations and acoustic excitations, but improvements in the numerical modeling of shocks and blade surface boundary conditions will be needed to improve the 2D LINFLUX predictions for unsteady transonic flows and unsteady flows excited by vortical gusts.

The main thrust of the present effort has been to provide a three-dimensional version of the LINFLUX analysis. The 3D linearized aerodynamic and numerical formulations are described in this report. A 3D version of the LINFLUX code has been constructed, based on these formulations, and applied to predict unsteady flows through relatively simple three-dimensional blade rows, i.e., a flat plate stator and a three-dimensional rotor that is an analog of the 10th Standard Cascade [FV93]. We have considered unsteady subsonic flows excited by blade vibrations and an unsteady flow excited by an acoustic plane wave that travels in the axial flow direction. We will present the LINFLUX results for these flows, along with results determined using TURBO, the two-dimensional, classical, linearized analysis of Smith [Smi72], and the two-dimensional, full-potential based linearization, LINFLO [Ver93].

Our predictions indicate that the current version of the 3D LINFLUX analysis provides qualitatively reasonable three-dimensional unsteady aerodynamic response information, but additional work will be needed to improve the predictions for unsteady flows excited by prescribed blade bending vibrations, and to reduce numerical losses near blade surfaces. In addition, accurate, three-dimensional, far-field, boundary conditions must be incorporated into the LINFLUX analysis, both to improve its flutter prediction capabilities and so that LINFLUX can be applied to unsteady flows driven by arbitrary external aerodynamic excitations. These issues will be addressed in our future work.

## 2. Unsteady Flow through a Blade Row

We consider time-dependent adiabatic flow, with negligible body forces, of an inviscid non-heat conducting perfect gas through a rotating blade row that operates within a stationary cylindrical annular duct of constant inner,  $r = r_H$ , and outer,  $r = r_D$ , radii (see Figure 2.1). The blade row consists of  $N$  distinct blades which rotate about the duct axis at constant angular velocity  $\Omega = \Omega e_\xi$ . In the absence of unsteady fluid dynamic forces, the blades are assumed to be identical in shape, identical in orientation relative to an axisymmetric inlet flow, and equally spaced around the rotor.

We will analyze this unsteady flow in a coordinate frame that rotates with the blading in terms of cylindrical  $(r, \theta, \xi, t)$  and Cartesian  $(x_1, x_2, x_3, t) = (\xi, r \sin \theta, -r \cos \theta, t)$  coordinates. Here  $\xi$  and  $r$  measure distance along and radially outward from the duct axis, respectively, and  $\theta$  measures angular distance in the direction opposite to the direction of rotation, which is assumed to be counterclockwise when looking in the axial flow direction. To describe flows in which the fluid domain varies with time it is useful to consider two sets of independent variables, say  $(\mathbf{x}, t)$  and  $(\bar{\mathbf{x}}, t)$ . The position vector  $\mathbf{x}(\bar{\mathbf{x}}, t) = \bar{\mathbf{x}} + \mathcal{R}(\bar{\mathbf{x}}, t)$  describes the instantaneous location of the moving field point,  $\bar{\mathbf{x}}$  refers to the reference or steady-state position of this point, and  $\mathcal{R}(\bar{\mathbf{x}}, t)$  is the displacement of the point from its reference position. The displacement field,  $\mathcal{R}$ , is prescribed so that the solution domain moves with solid boundaries and is stationary far from the blade row.

In the present discussion, all physical variables are dimensionless. Lengths have been scaled with respect to the reference length  $L^*$ , time with respect to the ratio  $L^*/V^*$  where  $V^*$  is the reference flow speed, velocity with respect to  $V^*$ , density with respect to a reference density  $\rho^*$ , pressure, with respect to  $\rho^*(V^*)^2$  and specific internal energy with respect to  $(V^*)^2$ . The superscript  $*$  refers to a dimensional reference value of a flow variable. The reference length is the axial blade chord, and the reference fluid density and flow speed are the inlet freestream, density and axial flow speed at blade midspan, respectively.

For aeroelastic and aeroacoustic applications we are usually interested in a restricted class of unsteady flows; those in which the unsteady fluctuations can be regarded as perturbations of a background flow that is steady in the blade row or rotor frame of reference. Thus, we consider situations in which the background flows far upstream (say  $\xi \leq \xi_-$ ) and far downstream ( $\xi \geq \xi_+$ ) from the blade row consist of at most a small steady perturbation from a steady, axisymmetric, swirling flow. The time-dependent or unsteady fluctuations in the flow arise from temporally and circumferentially periodic unsteady excitations of small-amplitude, i.e., prescribed vibratory blade motions and prescribed aerodynamic disturbances at inlet and exit that carry energy towards the blade row.

We will consider blade motions of the form

$$\mathcal{R}_{B_n}(\bar{r}, \bar{\theta} + 2\pi n/N, \bar{\xi}, t) = \mathbf{T}_n \text{Re}\{\mathbf{R}_B(\bar{r}, \bar{\theta}, \bar{\xi}) \exp[i(\omega t + n\sigma)]\}, \quad \bar{\mathbf{x}} \text{ on } B. \quad (2.1)$$

Here,  $\mathcal{R}_{B_n}$  is the displacement of a point on the  $n$ th moving blade surface relative to its mean position;  $\mathbf{T}_n$  is a rotation matrix, which relates a vector in the reference ( $n = 0$ ) passage to its counterpart in the  $n$ th passage;  $n = 0, 1, 2, \dots, N - 1$  is a blade number index;  $N$  is the number of blades in the row;  $\text{Re}\{ \}$  denotes the real part of  $\{ \}$ ;  $\mathbf{R}_B$  is the complex amplitude of the reference blade displacement;  $\omega$  is the (reduced) temporal frequency of the

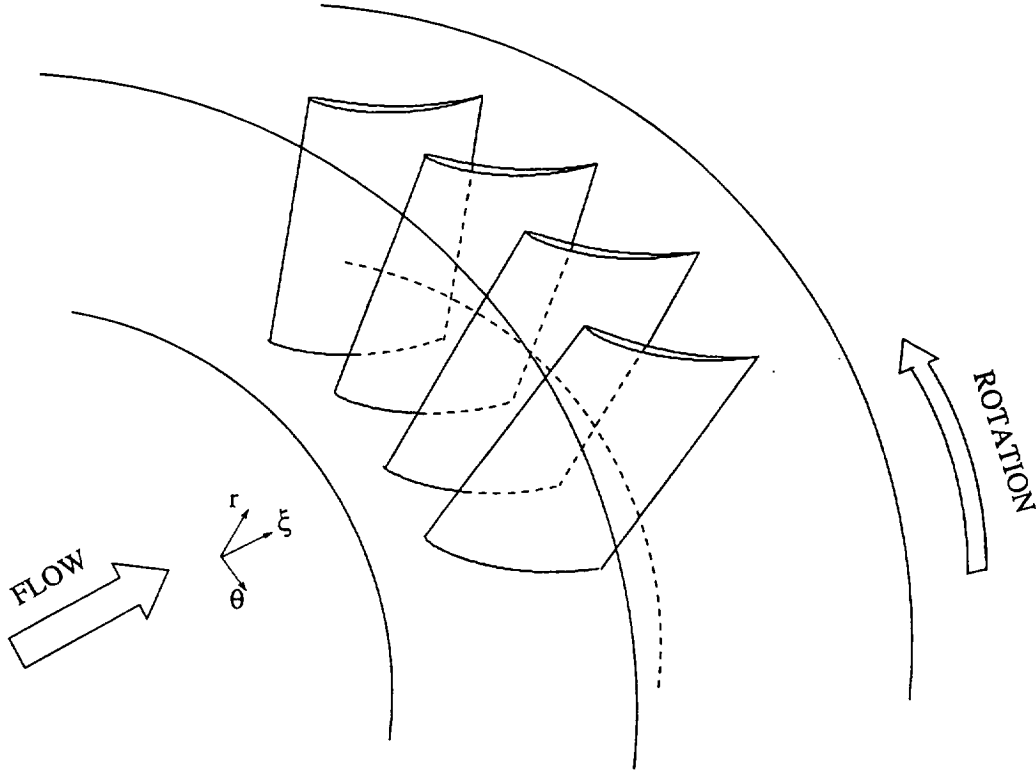


Figure 2.1: Rotating axial compressor blade row operating within a cylindrical duct.

blade motion;  $\sigma$  is the phase angle between the motions of adjacent blades; and  $B$  denotes mean position of the zeroth ( $n = 0$ ) or reference blade. The interblade phase angle,  $\sigma$ , is determined by the nodal diameter pattern of the vibratory motion, i.e.,  $\sigma = 2\pi N_D/N$ , where  $N_D$  is the integer count of the number of times a disturbance pattern repeats around the wheel. The sign of  $N_D$  is determined by the direction of rotation of the disturbance pattern; e.g., if  $N_D > 0$  the vibratory disturbance pattern moves in the direction of blade rotation, i.e., the negative  $\theta$ -direction.

The unsteady flows in the far upstream and far downstream regions are in part, prescribed as a fluid dynamic excitation and, in part, depend upon the interaction between the fluid and the blading. Typically, an unsteady aerodynamic excitation is represented as a linear combination of fundamental disturbances that are harmonic in time and in the circumferential direction. For example, a fundamental pressure excitation is of the form

$$\hat{p}_{I,\mp\infty}(\mathbf{x}, t) = \text{Re}\{p_{I,\mp\infty}(r) \exp[i(\omega t + m\theta) + \chi_m \xi]\}, \quad \xi \gtrless \xi_{\mp}. \quad (2.2)$$

Here,  $\hat{p}_{I,\mp\infty}(\mathbf{x}, t)$  is an incident pressure disturbance, i.e., a pressure disturbance that travels towards the blade row from far upstream ( $\xi \leq \xi_-$ ) or far downstream ( $\xi \geq \xi_+$ ),  $\omega$  is the temporal frequency of the disturbance, and  $|m|$  is the number of complete disturbance cycles that occur over one revolution, i.e., in the interval  $0 \leq \theta < 2\pi$ . The quantities  $\omega$  and  $m$  are prescribed, and  $p_{I,\mp\infty}(r)$  and  $\chi_m$  are determined from the equations that describe the fluid motion in the far field. The interblade phase angle,  $\sigma$ , of an incident disturbance is  $2\pi m/N$ .

### 3. Nonlinear Aerodynamic Equations

The field equations that govern the unsteady inviscid flow are derived from the conservation laws for mass, momentum and energy, and the thermodynamic relations for a perfect gas. If we consider a moving control volume,  $\mathcal{V}(t)$ , which is bounded by the control surface  $\mathcal{S}(\mathbf{x}, t) = 0$ , the conservation laws for the fluid within  $\mathcal{V}$  at time  $t$  can be written in column vector form as

$$\frac{d}{dt} \int_{\mathcal{V}} \tilde{\mathbf{U}} d\mathcal{V} + \int_{\mathcal{S}} [\tilde{\mathbf{F}}_j - \tilde{\mathbf{U}} \dot{\mathcal{R}}_{x_j}] n_{x_j} d\mathcal{S} = \int_{\mathcal{V}} \tilde{\mathbf{S}} d\mathcal{V}. \quad (3.1)$$

Here, the symbol  $\tilde{\cdot}$  indicates an unsteady flow variable,  $\dot{\mathcal{R}} = (\dot{\mathcal{R}}_{x_1}, \dot{\mathcal{R}}_{x_2}, \dot{\mathcal{R}}_{x_3})$  is the relative velocity of a field point lying on the control surface  $\mathcal{S}$ ,  $\mathbf{n}$  is the unit outward normal vector to the control surface, a summation over repeated indices is implied, and the source term on the right-hand-side of (3.1) accounts for the rotation of the reference frame that is fixed to the blade row.

The state,  $\tilde{\mathbf{U}}$ , flux,  $\tilde{\mathbf{F}}_j, j = 1, 2, 3$ , and source term,  $\tilde{\mathbf{S}}$ , vectors in (3.1) are defined by

$$\tilde{\mathbf{U}} = \begin{bmatrix} \tilde{\rho} \\ \tilde{\rho} \tilde{V}_{x_1} \\ \tilde{\rho} \tilde{V}_{x_2} \\ \tilde{\rho} \tilde{V}_{x_3} \\ \tilde{\rho} \tilde{E}_T \end{bmatrix}, \quad \tilde{\mathbf{F}}_j(\tilde{\mathbf{U}}) = \begin{bmatrix} \tilde{U}_{j+1} \\ \tilde{U}_{j+1} \tilde{U}_2 / \tilde{U}_1 + \tilde{P} \delta_{1j} \\ \tilde{U}_{j+1} \tilde{U}_3 / \tilde{U}_1 + \tilde{P} \delta_{2j} \\ \tilde{U}_{j+1} \tilde{U}_4 / \tilde{U}_1 + \tilde{P} \delta_{3j} \\ \tilde{U}_{j+1} (\tilde{U}_5 + \tilde{P}) / \tilde{U}_1 \end{bmatrix}, \quad \tilde{\mathbf{S}}(\tilde{\mathbf{U}}, \mathbf{x}) = \begin{bmatrix} 0 \\ 0 \\ \Omega^2 \tilde{U}_1 x_2 + 2\Omega \tilde{U}_4 \\ \Omega^2 \tilde{U}_1 x_3 - 2\Omega \tilde{U}_3 \\ \Omega^2 (\tilde{U}_3 x_2 + U_4 x_3) \end{bmatrix} \quad (3.2)$$

where  $\tilde{\rho}, \tilde{\mathbf{V}}, \tilde{E}_T = \tilde{E} + \tilde{V}^2/2$  and

$$\tilde{P} = (\gamma - 1) \tilde{\rho} \tilde{E} = (\gamma - 1) [\tilde{U}_5 - \tilde{U}_1^{-1} (\tilde{U}_2^2 + \tilde{U}_3^2 + \tilde{U}_4^2) / 2] \quad (3.3)$$

are the time-dependent fluid density, relative velocity, relative specific total internal energy, and pressure, respectively. As a convenience, we have expressed the flux vectors  $\tilde{\mathbf{F}}_j$  as explicit functions of the state variables  $\tilde{U}_i, i = 1, 2, \dots, 5$ , and the source term vector  $\tilde{\mathbf{S}}$  as an explicit function of the  $\tilde{U}_i$  and the spatial coordinates  $x_i, i = 1, 2, 3$ .

We can interchange the order of time differentiation and volume integration in (3.1) and convert the surface integral to a volume integral by applying Reynolds' transport and Green's theorems, respectively. Then, after taking the limit of the resulting volume integrals as  $\mathcal{V}(t) \rightarrow 0$ , we arrive at equations that describe the inviscid fluid motion at points within the fluid domain at which this motion is continuous and differentiable, i.e.,

$$\partial \tilde{\mathbf{U}} / \partial t \Big|_{\mathbf{x}} + \partial \tilde{\mathbf{F}}_j / \partial x_j = \tilde{\mathbf{S}}. \quad (3.4)$$

The foregoing field equations must be supplemented by conditions on the flow at the blade surfaces and duct walls and conditions at the inflow and outflow boundaries of the computational domain. Flow tangency conditions, i.e.,

$$(\tilde{\mathbf{V}} - \dot{\mathcal{R}}) \cdot \mathbf{n} = 0 \quad \text{for } \mathbf{x} \in \mathcal{B}_n \quad \text{and} \quad \tilde{\mathbf{V}} \cdot \mathbf{n} = 0 \quad \text{for } r = r_H, r_D, \quad (3.5)$$

apply at the moving blade surfaces and at the stationary duct walls, respectively. In addition, temporally- and circumferentially-averaged values of the total pressure, the total temperature

and the inlet flow angle are specified as functions of radius at the inflow boundary, and the circumferentially- and temporally-averaged pressure is specified at the outflow boundary, consistent with radial equilibrium. The unsteady fluctuations at inlet and exit that carry energy towards the blade row must also be specified; those that carry energy away from the blade row must be determined as part of the unsteady solution.

In principle, jump conditions, derived from the integral conservation laws (3.1), should be imposed at vortex-sheet wake and shock discontinuities. Such conditions are of the form

$$[[\tilde{\mathbf{F}}_j - \tilde{\mathbf{U}}\dot{\mathcal{R}}_{x_j}]]n_{x_j} = 0 \quad \text{for } \mathbf{x} \in W_n \quad \text{or } \mathbf{x} \in Sh_n, \quad (3.6)$$

where  $[[ \ ]]$  denotes the jump in a flow quantity across a surface of discontinuity and  $\dot{\mathcal{R}}$  is the surface velocity. However, the usual procedure in numerical calculations is to solve the conservative field equations (3.1) over the entire fluid domain in an attempt to “capture” wake and shock phenomena.

## 4. Linearized Unsteady Aerodynamic Model

Since the unsteady excitations are assumed to be of small amplitude (e.g.,  $|\mathcal{R}| \sim \mathcal{O}(\epsilon) \ll 1$ ), the unsteady part of the inviscid flow can be approximated as a first-order (in  $\epsilon$ ) perturbation of an underlying nonlinear background flow that is steady in the rotating frame of reference. Also, since the unsteady excitations are harmonic in time and the equations that govern the first-order flow properties will be linear, these properties will have harmonic time-dependence. We will take advantage of this feature by introducing frequency-domain representations for the first-order flow variables, thereby removing explicit physical time dependence from the resulting linearized unsteady problem.

To determine the small-disturbance equations, we first expand the unsteady state vector,  $\tilde{\mathbf{U}}$ , into an asymptotic series of the form

$$\tilde{\mathbf{U}}[\mathbf{x}(\bar{\mathbf{x}}, t)] = \mathbf{U}(\bar{\mathbf{x}}) + \tilde{\mathbf{u}}[\mathbf{x}(\bar{\mathbf{x}}, t), t] + \dots = \mathbf{U}(\bar{\mathbf{x}}) + \text{Re}[\mathbf{u}(\bar{\mathbf{x}}) \exp(i\omega t)] + \dots, \quad (4.1)$$

where the vector  $\mathbf{U}(\bar{\mathbf{x}}) \sim \mathcal{O}(1)$  contains the conservation variables for the steady background flow at  $\bar{\mathbf{x}}$ , the vector  $\tilde{\mathbf{u}}[\mathbf{x}(\bar{\mathbf{x}}, t), t] \sim \mathcal{O}(\epsilon)$  contains the conservation variables for the first-order unsteady flow at  $\mathbf{x}(\bar{\mathbf{x}}, t) = \bar{\mathbf{x}} + \mathcal{R}(\bar{\mathbf{x}}, t) = \bar{\mathbf{x}} + \text{Re}\{\mathbf{R}(\bar{\mathbf{x}}) \exp(i\omega t)\}$ , and the dots refer to higher order terms. The components of the vector  $\mathbf{u}$  are the complex amplitudes of the linearized unsteady conservation variables, i.e.,

$$\mathbf{u}^T = [\rho, \bar{\rho}v_{x_1} + \rho V_{x_1}, \bar{\rho}v_{x_2} + \rho V_{x_2}, \bar{\rho}v_{x_3} + \rho V_{x_3}, \bar{\rho}e_T + \rho E_T] \quad (4.2)$$

where  $\bar{\rho}$ ,  $\mathbf{V}$  and  $E_T$  and  $\rho$ ,  $\mathbf{v}$ , and  $e_T$  are the steady and the complex amplitudes of the first-order unsteady flow variables, respectively.

The asymptotic expansion (4.1) is based on an independent variable transformation,  $(\mathbf{x}, t) \rightarrow (\bar{\mathbf{x}}, t)$ , suggested by Hall and Clark [HC93a] and by Giles [Gil93]. This transformation from the instantaneous,  $\mathbf{x}$ , to the stationary,  $\bar{\mathbf{x}}$ , spatial coordinates contains the information that describes the blade motion and the corresponding field deformation. It allows linearized unsteady flow solutions to be determined over a fixed domain or grid in physical space without introducing difficult extrapolation terms into the blade surface conditions. However, source terms, resulting from the grid deformation, appear in the linearized unsteady field equation.

As a consequence of the assumptions regarding rotor geometry, inlet and exit mean-flow conditions, and the temporal and circumferential behaviors of the unsteady excitations, the steady background flow will be periodic from blade-to-blade, and the first-order unsteady flow will exhibit a phase-lagged, blade-to-blade periodicity. Thus, e.g., we can write

$$\mathbf{V}(\bar{r}, \bar{\theta} + 2\pi n/N, \bar{\xi}) = \mathbf{T}_n \mathbf{V}(\bar{r}, \bar{\theta}, \bar{\xi}) \text{ and } \mathbf{v}(\bar{r}, \bar{\theta} + 2\pi n/N, \bar{\xi}) = \mathbf{T}_n \mathbf{v}(\bar{r}, \bar{\theta}, \bar{\xi}) \exp(in\sigma), \quad (4.3)$$

where the matrix  $\mathbf{T}_n$  rotates a velocity vector through  $n$  passages. The conditions in (4.3) allow numerical resolutions of the steady and linearized unsteady flows to be limited to a single extended blade-passage region, i.e., a region of angular pitch  $\Delta\theta = 2\pi/N$ .

The unsteady flux  $\tilde{\mathbf{F}}_j$  and source term,  $\tilde{\mathbf{S}}$ , vectors can be approximated using Taylor series expansions about the mean flow state,  $\mathbf{U}$ , and the reference spatial location,  $\bar{\mathbf{x}}$ , i.e.,

$$\tilde{\mathbf{F}}_j(\tilde{\mathbf{U}}) = \mathbf{F}_j(\mathbf{U}) + \frac{\partial \mathbf{F}_j}{\partial \mathbf{U}} \tilde{\mathbf{u}} + \dots \quad \text{and} \quad \tilde{\mathbf{S}}(\tilde{\mathbf{U}}, \mathbf{x}) = \mathbf{S}(\mathbf{U}, \bar{\mathbf{x}}) + \frac{\partial \mathbf{S}}{\partial \mathbf{U}} \tilde{\mathbf{u}} + (\mathcal{R} \cdot \nabla_{\bar{\mathbf{x}}}) \mathbf{S} + \dots \quad (4.4)$$

Here  $\partial \mathbf{F}_j / \partial \mathbf{U} = \{\partial F_{ij} / \partial U_k\}$  and  $\partial \mathbf{S} / \partial \mathbf{U} = \{\partial S_i / \partial U_k\}$  are Jacobian matrices and the subscripts  $i$  and  $k$  refer to the  $i$ th row and  $k$ th column, respectively, of these matrices.

We have expressed the nonlinear fluid dynamic equations (3.4) in terms of the independent variables  $\mathbf{x}$  and  $t$ . However, the use of dependent variable expansions of the form (4.1) renders it necessary to express the steady and linearized unsteady equations in terms of the independent variables  $\bar{\mathbf{x}}$  and  $t$ . To within first-order, the transformation relations are

$$\partial / \partial t|_{\mathbf{x}} = \partial / \partial t|_{\bar{\mathbf{x}}} - (\dot{\mathbf{R}} \cdot \nabla_{\bar{\mathbf{x}}}) + \dots \quad \text{and} \quad \partial / \partial x_j = \partial / \partial \bar{x}_j - (\partial \mathcal{R}_m / \partial \bar{x}_j) \partial / \partial \bar{x}_m + \dots \quad (4.5)$$

The equations that govern the zeroth-order steady and the first-order unsteady flows are then obtained by substituting the expansions (4.1), (4.4) and (4.5) into the nonlinear governing equations; equating terms of like power in  $\epsilon$ ; and neglecting terms of second and higher order in  $\epsilon$ . This procedure leads to nonlinear and linear variable-coefficient equations, respectively, for the zeroth- and first-order flows. The variable coefficients that appear in the linearized equations depend upon the steady background flow.

The differential conservation equation for the steady background flow is

$$\partial \mathbf{F}_j / \partial \bar{x}_j = \mathbf{S} . \quad (4.6)$$

In addition, the condition  $\mathbf{V} \cdot \mathbf{n} = 0$  applies at the blade surfaces ( $\bar{\mathbf{x}} \in B_n$ ), and the duct walls ( $r = r_H$  and  $r = r_D$ ), and a periodic condition on  $\mathbf{U}$ , cf. (4.3), applies upstream and downstream of the blade row. Circumferentially averaged values of the appropriate mean flow variables are specified as functions of radius at the inflow and outflow boundaries and circumferential harmonics of these variables are allowed to evolve to values that are consistent with a blade row operating within an infinite annular duct.

The field equation that governs the first-harmonic unsteady perturbation can be written as

$$\begin{aligned} i\omega \mathbf{u} + \frac{\partial}{\partial \bar{x}_j} \left( \frac{\partial \mathbf{F}_j}{\partial \mathbf{U}} \mathbf{u} \right) - \frac{\partial \mathbf{S}}{\partial \mathbf{U}} \mathbf{u} &= \frac{\partial}{\partial \bar{x}_j} (R_{x_j} \mathbf{S}) - i\omega \frac{\partial R_{x_m}}{\partial \bar{x}_m} \mathbf{U} \\ &+ \frac{\partial}{\partial \bar{x}_j} \left[ i\omega (R_{x_j} \mathbf{U}) + \frac{\partial R_{x_j}}{\partial x_m} \mathbf{F}_m - \frac{\partial R_{x_m}}{\partial \bar{x}_m} \mathbf{F}_j \right], \end{aligned} \quad (4.7)$$

where the terms that depend explicitly on the displacement field resulting from the blade vibration, i.e., on  $\mathbf{R}$ , are regarded as source terms. The linearized flow tangency conditions at the moving blade surfaces and the stationary ( $\mathbf{R} \equiv 0$ ) duct walls are given by

$$\mathbf{v} \cdot \mathbf{n} = i\omega \mathbf{R} \cdot \mathbf{n} + \mathbf{V} \cdot \nabla (\mathbf{R} \cdot \mathbf{n}), \quad \text{for } \bar{\mathbf{x}} \in B_n, \quad r = r_H \text{ and } r = r_D . \quad (4.8)$$

In addition, phase-lagged periodicity, cf. (4.3), and analytic far-field conditions must be imposed. The latter must allow for the prescription of the various unsteady aerodynamic excitations and permit unsteady disturbances coming from within the solution domain to pass through the inlet and exit boundaries without reflection.

For a numerical integration of the steady and linearized unsteady boundary value problems, it is advantageous to regard the state vectors  $\mathbf{U}$  and  $\mathbf{u}$  as pseudo time dependent, i.e., to set  $\mathbf{U} = \mathbf{U}(\bar{\mathbf{x}}, \tau)$  and  $\mathbf{u} = \mathbf{u}(\bar{\mathbf{x}}, \tau)$ , where  $\tau$  is the pseudo time variable, and include the terms  $\partial \mathbf{U} / \partial \tau|_{\bar{\mathbf{x}}}$  and  $\partial \mathbf{u} / \partial \tau|_{\bar{\mathbf{x}}}$  on the left-hand sides of (4.6) and (4.7), respectively.

This allows conventional time-marching algorithms to be used to converge solutions for the steady and the complex amplitudes of the unsteady conservation variables to steady-state values. Also, for a finite-volume calculation, the integral forms of (4.6) and (4.7) are required. These may be found by a direct integration of (4.6) and (4.7) over a fixed volume,  $V$ , and bounding control surface,  $S(\bar{\mathbf{x}})$ , in reference physical space, or by a direct application of the small-unsteady-disturbance approximations to the integral equation (3.1).

If we include the pseudo-time derivative terms on the left hand sides, the integral conservation equations for the steady background and the first-harmonic unsteady flows have the form

$$\frac{d}{d\tau} \int_V \mathbf{U} dV + \int_S \mathbf{F}_j n_{x_j} dS = \int_V \mathbf{S} dV \quad (4.9)$$

and

$$\begin{aligned} & \left( \frac{\partial}{\partial \tau} + i\omega \right) \int_V \mathbf{u} dV + \int_S \left( \frac{\partial \mathbf{F}_j}{\partial \mathbf{U}} \mathbf{u} \right) n_{x_j} dS - \int_V \frac{\partial \mathbf{S}}{\partial \mathbf{U}} \mathbf{u} dV \\ & = \int_V \left[ \frac{\partial}{\partial \bar{x}_j} (R_{x_j} \mathbf{S}) - i\omega \left( \frac{\partial R_{x_m}}{\partial \bar{x}_m} \right) \mathbf{U} \right] dV \\ & + \int_S \left[ i\omega R_{x_j} \mathbf{U} + \frac{\partial R_{x_j}}{\partial \bar{x}_m} \mathbf{F}_m - \left( \frac{\partial R_{x_m}}{\partial \bar{x}_m} \right) \mathbf{F}_j \right] n_{x_j} dS . \end{aligned} \quad (4.10)$$

To determine unsteady flows excited by prescribed blade motions, the displacement field,  $\mathbf{R}(\bar{\mathbf{x}})$  in (4.10), must be prescribed throughout the solution domain, i.e., a single, extended, blade-passage region of finite axial extent. This field should be defined so that the deforming physical solution domain conforms to the motions of the blades, i.e., a field point on a moving blade surface should have the same  $\bar{\mathbf{x}}$ -coordinate for all time. Throughout the remainder of the computational domain, the displacement field can be defined in whatever manner is most convenient for implementing the flow boundary conditions. In the present study,  $\mathbf{R}(\bar{\mathbf{x}})$  is determined as a solution of Laplace's equation,  $\nabla_{\bar{\mathbf{x}}}^2 \mathbf{R} = \mathbf{0}$ , subject to Dirichlet boundary conditions at the blade surfaces (i.e.,  $\mathbf{R}(\bar{\mathbf{x}}) = \mathbf{R}_{B_n}(\bar{\mathbf{x}})$  for  $\bar{\mathbf{x}} \in B_n$ ), the duct walls ( $\mathbf{R}(\bar{\mathbf{x}}) = \mathbf{0}$  for  $\bar{r} = r_H, r_D$ ), and in the far field ( $\mathbf{R}(\bar{\mathbf{x}}) = \mathbf{0}$  for  $\bar{\xi} \lesssim \bar{\xi}_{\mp}$ ), and phase-lagged, blade-to-blade, periodicity conditions [i.e.,  $\mathbf{R}(\bar{r}, \bar{\theta} + 2\pi/N, \bar{\xi}) = \mathbf{T}_1 \mathbf{R}(\bar{r}, \bar{\theta}, \bar{\xi}) \exp(i\sigma)$ ] upstream and downstream of the blade row.

## 5. Numerical Model for the Linearized Equations

The field equations that govern the nonlinear steady and the first-harmonic, linearized, unsteady flows through a blade row rotating at constant angular velocity  $\Omega$  have been given in differential form, as equations (4.6) and (4.7), respectively, and in integral form, with pseudo time dependence added, as equations (4.9) and (4.10). The unsteady equation has been written in a conservation form in which the terms that depend explicitly on the blade motion, i.e., on  $\mathbf{R}$ , are regarded as known source terms. The steady and linearized unsteady field equations must be solved, in sequence, subject to appropriate boundary conditions at the blade surfaces and the duct walls, and at the blade-to-blade periodic boundaries and the inflow and outflow boundaries of the computational domain, as described in §4.

We proceed to describe the numerical procedures developed to resolve linearized, harmonic, unsteady flows. These procedures are based on those used in the nonlinear unsteady analysis TURBO, and have been implemented into an unsteady flow code called LINFLUX. TURBO is an implicit, flux-split, cell-centered, finite-volume analysis that can be used to predict three-dimensional, nonlinear, inviscid and viscous, unsteady flows through blade rows. A detailed description can be found in [JHW92]. Also, an excellent description of the basic numerical method underlying TURBO and its two-dimensional counterpart, called NPHASE, can be found in [SLH<sup>+</sup>94]. The TURBO analysis is applied in the present study to provide the steady background flow information needed for a linearized inviscid analysis.

The computational mesh used in the TURBO and LINFLUX analyses is a sheared H-mesh, typically generated using the TIGER grid generation package [SS91]. This structured mesh defines a curvilinear coordinate system, the boundaries of which lie along the boundaries of the physical domain, such that there is a one-to-one correspondence from points,  $\bar{\mathbf{x}}$ , in the physical domain to points,  $\alpha$ , in a rectangular computational domain, where the grid is uniform and orthogonal.

For a finite volume discretization, the geometrical properties of the mesh cells in physical space are required. These properties are computed from the locations of the cell vertices in physical space. The mesh points in physical space define the eight vertices of the non-overlapping hexahedral cells which fill the physical solution domain. Cell faces are surfaces of constant computational coordinate, so that each cell is bounded by the six surfaces, say  $\alpha_1 = I - 1/2, I + 1/2$  and  $\alpha_2 = J - 1/2, J + 1/2$  and  $\alpha_3 = K - 1/2, K + 1/2$ . The connectivity of the cells is thus known from the computational coordinates, with neighboring cells given by changing a computational coordinate by one. Because of the transformation  $(\mathbf{x}, t) \rightarrow (\bar{\mathbf{x}}, t)$ , the geometric terms required to define the spatial discretization are independent of time. This means that the mean cell volumes and face areas are used in computing the linearized unsteady flow.

### 5.1 Finite Volume Equations

Let the symbol  $\hat{\cdot}$  refer to a quantity expressed in terms of the mean cell geometry, i.e., in terms of  $\bar{v}$ , the mean cell volume, or  $\bar{A}_{j,k}$ , the mean area of the constant  $\alpha_j$  cell face projected in the  $\bar{x}_k$  direction. Then, the finite-volume spatial discretization of the linearized unsteady

equation (4.10) can be written as

$$\left. \frac{\partial \hat{\mathbf{u}}}{\partial \tau} \right|_{\alpha} = -i\omega \hat{\mathbf{u}} - \delta_j \hat{\mathbf{f}}_j + \frac{\partial \mathbf{S}}{\partial \mathbf{U}} \hat{\mathbf{u}} - i\omega(\Delta\vartheta)\mathbf{U} - \delta_j \hat{\mathbf{f}}_j^d + (\Delta\vartheta)\mathbf{S} + \bar{\vartheta}(\mathbf{R} \cdot \nabla_{\bar{\mathbf{x}}})\mathbf{S} = -\hat{\mathbf{r}} \quad (5.1)$$

where

$$\hat{\mathbf{u}} = \bar{\vartheta} \mathbf{u}, \quad \hat{\mathbf{f}}_j = \frac{\partial \hat{\mathbf{F}}_j}{\partial \mathbf{U}} \mathbf{u} = \bar{A}_{jk} \frac{\partial \mathbf{F}_k}{\partial \mathbf{U}} \mathbf{u} = \bar{A}_{jk} \mathbf{f}_k, \quad \text{and} \quad \hat{\mathbf{f}}_j^d = -\dot{\vartheta}_j \mathbf{U} + a_{jk} \mathbf{F}_k. \quad (5.2)$$

In equations (5.1) and (5.2),  $\mathbf{U}$ ,  $\mathbf{u}$ , and  $\mathbf{S}$  represent average values of the physical state and source term vectors over the mean cell volume, the vectors  $\hat{\mathbf{F}}_j$  and  $\hat{\mathbf{f}}_j$  are the steady and unsteady perturbation fluxes, respectively, across a constant  $\alpha_j$  face,  $\hat{\mathbf{f}}_j^d$  is the unsteady flux across the constant  $\alpha_j$  face associated with the deformation field,  $\mathbf{R}$ , and  $\hat{\mathbf{r}}$  is the residual of the first-harmonic unsteady equation. The steady quantities  $\bar{\vartheta}$ ,  $\bar{A}_{jk}$ ,  $\mathbf{U}$ ,  $\mathbf{F}_j(\mathbf{U})$  and  $\mathbf{S}(\mathbf{U})$  are regarded as known in the unsteady analysis. The operator  $\delta_j$  in (5.1) represents the difference, in the  $\alpha_j$ -direction, across adjacent cell interfaces, e.g.,  $\delta_j(\ )|_J = (\ )_{j,J+1/2} - (\ )_{j,J-1/2}$ , where  $J$  is a cell index, the  $J \pm 1/2$  are the corresponding cell-face indices, and the repeated  $j$  index implies summation over all computational coordinate directions, so that the term  $(\delta_j \hat{\mathbf{f}}_j)_J$  is the net flux through the  $J$ th cell.

The linearized perturbation equation contains source terms that arise because this equation has been expressed in terms of the reference spatial coordinates,  $\bar{\mathbf{x}}$ . The source terms depend on known steady flow properties and on the prescribed displacement field,  $\mathbf{R}(\bar{\mathbf{x}})$ . They are associated with changes in cell volume, cell face area, and cell radial location. The volume source term is given by  $-i\omega(\Delta\vartheta)\mathbf{U} + (\Delta\vartheta)\mathbf{S}$ , where  $\Delta\vartheta = \delta_j(\bar{A}_{jk} R_{x_k})$  is the complex amplitude of the first-harmonic perturbation in the cell volume. The cell, face-area, source term,  $\hat{\mathbf{f}}_j^d$ , is defined in equation (5.2), and accounts for the mean flux through the moving cell faces. The complex amplitudes of the first-harmonic perturbations in the projected face areas,  $a_{jk}$ , are computed using first order expansions in  $\mathbf{R}$  for the area of a cell face. The swept volume is given by  $\dot{\vartheta}_j = i\omega \bar{A}_{jk} R_{x_k}$ . In evaluating  $\Delta\vartheta$  and  $\dot{\vartheta}_j$  the  $R_{x_k}$  are taken to be the average displacements over a cell face. The remaining grid deformation source term,  $\bar{\vartheta}(\mathbf{R} \cdot \nabla_{\bar{\mathbf{x}}})\mathbf{S}$ , where  $\mathbf{R}$  is based on the average displacement of the cell vertices, accounts for changes in radial location.

The field equation (5.1) must be solved subject to the conditions imposed at the boundaries of the computational domain. Flow tangency conditions, cf. (4.8), apply at the blade surfaces and the duct walls, a phase-lagged, periodicity condition, cf. (4.3), is applied at the blade-to-blade periodic boundaries and analytic far-field conditions are applied at the inflow and outflow boundaries. The far-field conditions must allow for the prescription of external aerodynamic disturbances and permit unsteady disturbance waves coming from within the solution domain to pass through the inflow and outflow boundaries without reflection. The far-field conditions currently used in LINFLUX are based on one-dimensional characteristic theory. This severely limits the external aerodynamic excitations that can be considered to those occurring at near zero interblade phase angle, and relies on the dissipative nature of an axially stretched mesh to damp oblique outgoing disturbances.

### *Pseudo-Time Marching Procedure*

A pseudo-time marching technique is used to converge successive estimates for the complex amplitudes of the unsteady conservation variables to constant or “steady-state” values. For this purpose, the pseudo time derivative in (5.1) is approximated using a first-order accurate, two-point, backward, difference approximation. In particular, we set

$$\hat{\Theta} \Delta \mathbf{u}^n = -\hat{\mathbf{r}}^{n+1} , \quad (5.3)$$

where the superscript  $n$  refers to the current or  $n$ th pseudo time level,  $\hat{\Theta} = \bar{\vartheta} / \Delta \tau$ ,  $\Delta \mathbf{u}^n = (\mathbf{u}^{n+1} - \mathbf{u}^n)$  is a pseudo-time update to the state vector, and the norm  $\|\Delta \mathbf{u}^n\|$  is expected to approach zero with increasing  $n$ . Equation (5.3) is used to determine the state vector  $\mathbf{u}^{n+1}$  at the  $(n + 1)$ th time step in terms of the state vector at the previous time step, and unsteady residual,  $\hat{\mathbf{r}}$ , at the  $(n + 1)$ th time step. The unsteady residual is a linear function of the state vector  $\mathbf{u}$ .

After expanding the residual,  $\hat{\mathbf{r}}^{n+1}$ , about the  $n$ th time level, we can write the discretized unsteady field equation as

$$\left( \hat{\Theta} \mathbf{I} + \left. \frac{\partial \hat{\mathbf{r}}}{\partial \mathbf{u}} \right|^n \right) (\mathbf{u}^{n+1} - \mathbf{u}^n) = -\hat{\mathbf{r}}^n , \quad (5.4)$$

where  $\hat{\mathbf{r}}^n$  is defined in (5.1), and the change in the residual due to the pseudo-time update is given by

$$\left. \frac{\partial \hat{\mathbf{r}}}{\partial \mathbf{u}} \right|^n \Delta \mathbf{u}^n = i\omega \bar{\vartheta} \Delta \mathbf{u}^n + \delta_j \left[ \left. \frac{\partial \hat{\mathbf{F}}_j}{\partial \mathbf{U}} \right|^n \Delta \mathbf{u}^n \right] - \bar{\vartheta} \left. \frac{\partial \mathbf{S}}{\partial \mathbf{U}} \right|^n \Delta \mathbf{u}^n . \quad (5.5)$$

It follows from (5.3)–(5.5) that the pseudo-time update formula can be expressed in the form

$$\left( \hat{\Theta} + i\omega \bar{\vartheta} - \bar{\vartheta} \left. \frac{\partial \mathbf{S}}{\partial \mathbf{U}} \right|^n \right) \Delta \mathbf{u}^n + \delta_j \left[ \left. \frac{\partial \hat{\mathbf{F}}_j}{\partial \mathbf{U}} \right|^n \Delta \mathbf{u}^n \right] = -\bar{\vartheta} \left( i\omega - \left. \frac{\partial \mathbf{S}}{\partial \mathbf{U}} \right|^n \right) \mathbf{u}^n - (\delta_j \hat{\mathbf{f}}_j)^n + \mathbf{s}^n = -\hat{\mathbf{r}}^n , \quad (5.6)$$

where  $\mathbf{s}$  is the grid deformation source term.

## 5.2 Evaluation of Flux Terms

In this and the following subsections we will describe the spatial discretizations that are used to approximate the flux terms on the left- and right-hand sides of equation (5.6) and the pseudo-time integration used to solve this equation. To simplify these descriptions, we will consider a “one-dimensional flow” in which  $\hat{\mathbf{F}}_j = \hat{\mathbf{F}}$  and  $\hat{\mathbf{f}}_j = \hat{\mathbf{f}}$  are the steady and unsteady flux vectors in the  $\alpha_j = \alpha$  computational coordinate direction. The subscript  $J$  will refer to the cell volume bounded by the constant  $\alpha$ -surfaces at  $J + 1/2$  and  $J - 1/2$ . The extensions of the equations that follow to three-dimensional flows is straightforward conceptually, but involves the use of considerable and tedious nomenclature.

## Interfacial Fluxes

A cell-centered finite-volume discretization requires that the fluxes at cell surfaces be computed in terms of the values of the state vector in the neighboring cell volumes. In the TURBO and LINFLUX analyses, a flux splitting technique is applied in which the flux at a cell interface is computed in terms of a flux Jacobian matrix representing the local interface conditions and the values of the state vector in the cell volumes adjacent to the interface. The eigenvalues of the flux Jacobian matrix are used to determine which characteristic modes are taken into account, thus controlling the direction of spatial differencing. This technique results in first-order spatial accuracy. Higher order accuracy is achieved by adding corrective fluxes to the first-order discrete approximations for the interfacial fluxes.

The flux splitting is based on a similarity transformation and an eigenvalue decomposition of the physical flux Jacobian matrix,  $\partial\mathbf{F}/\partial\mathbf{U}$ , into matrices that account for right (+) and left (-) traveling disturbances. Thus, the flux vector,  $\mathbf{f}$ , is split according to

$$\mathbf{f} = \frac{\partial\mathbf{F}}{\partial\mathbf{U}}\mathbf{u} = \left( \frac{\partial\mathbf{F}^+}{\partial\mathbf{U}} + \frac{\partial\mathbf{F}^-}{\partial\mathbf{U}} \right) \mathbf{u} = \mathbf{T}(\Lambda^+ + \Lambda^-) \mathbf{T}^{-1}\mathbf{u} \quad (5.7)$$

with the (+) terms being determined using information from the negative coordinate direction and the (-) terms, using information from the positive coordinate direction. The matrices  $\mathbf{T}$  and  $\mathbf{T}^{-1}$  contain the right and left eigenvectors, respectively, of  $\partial\mathbf{F}/\partial\mathbf{U}$ ,  $\Lambda$  is the diagonal matrix of eigenvalues, and  $\Lambda^+$  and  $\Lambda^-$  are diagonal matrices containing the positive (+) and negative (-) eigenvalues, respectively. The sign of the wave speed (i.e., + or -) determines the direction in which spatial differencing is applied.

In the TURBO analysis, two methods are applied to evaluate surface fluxes. One is the flux vector splitting scheme proposed by Steger and Warming [SW81]; the other, the flux difference splitting scheme proposed by Roe [Roe81]. The former is applied to evaluate the left-hand-side flux terms in (5.6); the latter, to evaluate those on the right-hand side. Flux vector splitting is used in the nonlinear analysis, because the resulting flux Jacobians are easier to compute than those resulting from flux difference splitting. However, in LINFLUX, flux difference splitting is used to evaluate the flux terms on both sides of the linear unsteady equation. This is feasible because the steady flux Jacobian matrices must only be computed once, and it has been found to improve the convergence rates of linear unsteady solutions.

In the flux difference splitting approach, the flux,  $\hat{\mathbf{f}}_{J+1/2}$ , at the  $J + 1/2$  cell interface is constructed from the flux in the cell to the left ( $J$ ) or right ( $J + 1$ ) of the interface plus the flux due to waves approaching the interface due to the change in the state vector across the interface. In the present implementation, we have chosen to evaluate the flux vector,  $\hat{\mathbf{f}}_{J+1/2}$ , based on  $\hat{\mathbf{f}}(\mathbf{u}_J)$ , and disturbances traveling to the left, i.e., at negative wave velocity. This results an approximate expression for the unsteady flux at the  $J + 1/2$  interface of the form

$$\hat{\mathbf{f}}_{J+1/2} = \left( \frac{\partial\hat{\mathbf{F}}}{\partial\mathbf{U}}\mathbf{u} \right)_{J+1/2} \approx \hat{\mathbf{f}}(\mathbf{u}_J)|_{J+1/2} + \left( \frac{\partial\hat{\mathbf{F}}}{\partial\mathbf{U}} \Big|_{\mathbf{U}=\mathbf{U}_{J+1/2}^{\text{Roe}}} \right)^- (\mathbf{u}_{J+1} - \mathbf{u}_J), \quad (5.8)$$

where  $\hat{\mathbf{f}}(\mathbf{u}_J)|_{J+1/2}$  is a flux based on the state vector in the  $J$ th cell, the area used in calculating the flux terms on the right-hand side of (5.8) is that at the  $J + 1/2$  interface, and the

intermediate state vector,  $\mathbf{U}_{J+1/2}^{\text{Roe}}$ , is based on  $\mathbf{U}_J$  and  $\mathbf{U}_{J+1}$  and defined using the relations:

$$\bar{\rho}_{J+1/2}^{\text{Roe}} = \sqrt{\bar{\rho}_J \bar{\rho}_{J+1}}, \quad \mathbf{V}_{J+1/2}^{\text{Roe}} = \frac{\sqrt{\bar{\rho}_J} \mathbf{V}_J + \sqrt{\bar{\rho}_{J+1}} \mathbf{V}_{J+1}}{\sqrt{\bar{\rho}_J} + \sqrt{\bar{\rho}_{J+1}}},$$

and

$$E_{T,J+1/2}^{\text{Roe}} = \frac{\sqrt{\bar{\rho}_J} E_{T,J} + \sqrt{\bar{\rho}_{J+1}} E_{T,J+1}}{\sqrt{\bar{\rho}_J} + \sqrt{\bar{\rho}_{J+1}}}.$$

The flux,  $\hat{\mathbf{f}}_{J+1/2}$ , in (5.8) could have been constructed from  $\hat{\mathbf{f}}(\mathbf{u}_{J+1})|_{J+1/2}$  and the disturbances traveling at positive wave velocity, or from an average value of the flux vectors in the neighboring cells and an average of the disturbances traveling at positive and negative wave velocities.

The discrete approximation (5.8) is first-order accurate, since the interfacial fluxes are based only upon information from adjacent cells. Higher order spatial accuracy can be achieved by adding corrective fluxes, which bring in information from additional neighboring cells. In TURBO, flux limiters are used in conjunction with the corrective fluxes to control the dispersive errors that occur near shocks and stagnation points. Such limiters have not yet been incorporated into the LINFLUX analysis.

The corrective perturbation flux at the  $J + 1/2$  interface is comprised of right traveling waves at the upstream interface ( $J - 1/2$ ) of the adjacent upstream cell ( $J$ ) and left traveling waves at the downstream interface ( $J + 3/2$ ) of the adjacent downstream cell ( $J + 1$ ). These waves are approximated using the Roe-averaged flux Jacobian matrix at the  $J + 1/2$  interface. Thus, the enhanced approximation to the perturbation flux is given by

$$\begin{aligned} \hat{\mathbf{f}}_{J+1/2} \approx & \hat{\mathbf{f}}(\mathbf{u}_J)|_{J+1/2} + \left( \frac{\partial \hat{\mathbf{F}}}{\partial \mathbf{U}} \Big|_{\mathbf{U}=\mathbf{U}_{J+1/2}^{\text{Roe}}} \right)^- (\mathbf{u}_{J+1} - \mathbf{u}_J) \\ & + \frac{1}{2} \left[ \left( \frac{\partial \hat{\mathbf{F}}}{\partial \mathbf{U}} \Big|_{\mathbf{U}=\mathbf{U}_{J+1/2}^{\text{Roe}}} \right)^+ (\mathbf{u}_J - \mathbf{u}_{J-1}) - \left( \frac{\partial \hat{\mathbf{F}}}{\partial \mathbf{U}} \Big|_{\mathbf{U}=\mathbf{U}_{J+1/2}^{\text{Roe}}} \right)^- (\mathbf{u}_{J+2} - \mathbf{u}_{J+1}) \right], \end{aligned} \quad (5.10)$$

and results in second order spatial accuracy.

### *Right- and Left-Hand-Side Flux Terms*

Once the interfacial fluxes have been computed, they are spatially differenced to compute the flux terms that appear on the right- and left-hand sides of the unsteady equation (5.6). The difference expression for the net unsteady flux through the  $J$ th control volume is

$$\delta \hat{\mathbf{f}}|_J \approx \hat{\mathbf{f}}_{J+1/2} - \hat{\mathbf{f}}_{J-1/2}, \quad (5.11)$$

and the second-order discrete approximation in (5.10) is used to evaluate the interfacial fluxes on the right-hand side of (5.11). The left-hand side flux term in (5.6) represents the

change in the net unsteady flux due to the pseudo time update. It is evaluated using the first-order accurate flux difference splitting approximation in (5.8), i.e.,

$$\begin{aligned} \delta_j \left( \frac{\partial \hat{\mathbf{F}}}{\partial \mathbf{U}} \Delta \mathbf{u} \right) \Big|_J &\approx \hat{\mathbf{f}}(\Delta \mathbf{u}_J) \Big|_{J+1/2} + \frac{\partial \hat{\mathbf{F}}}{\partial \mathbf{U}} \Big|_{\mathbf{U}=\mathbf{U}_{J+1/2}^{\text{Roe}}}^- (\Delta \mathbf{u}_{J+1} - \Delta \mathbf{u}_J) \\ &- \hat{\mathbf{f}}(\Delta \mathbf{u}_{J-1}) \Big|_{J-1/2} - \frac{\partial \hat{\mathbf{F}}}{\partial \mathbf{U}} \Big|_{\mathbf{U}=\mathbf{U}_{J-1/2}^{\text{Roe}}}^- (\Delta \mathbf{u}_J - \Delta \mathbf{u}_{J-1}), \end{aligned} \quad (5.12)$$

where  $\hat{\mathbf{f}}(\Delta \mathbf{u}_J) \Big|_{J+1/2} = \partial \mathbf{F} / \partial \mathbf{U} \Big|_{\mathbf{U}=\mathbf{U}_J} A_{J+1/2} \Delta \mathbf{u}_J = (\partial \hat{\mathbf{F}} / \partial \mathbf{U})_{J,J+1/2} \Delta \mathbf{u}_J$ . Thus, when expressing flux Jacobians with two subscripts, the first subscript refers to the cell where the state vector is evaluated and the second refers to the cell face where the area is evaluated.

### 5.3 Pseudo-Time Integration

The linearized unsteady equation (5.6) is discretized, as outlined above, leading to a linear system of algebraic equations. In this discretization, the flux terms on both the left- and right-hand-sides of equation (5.6) are computed using flux difference splitting and the approximations to the flux terms on the right-hand-side are corrected for higher order spatial accuracy. The resulting system of algebraic equations is solved at each pseudo-time step using an iteration procedure in which the left-hand side matrix is decomposed into diagonal and off-diagonal, positive and negative, submatrices. Symmetric Gauss-Seidel (SGS) iterations [WT91] are then applied to solve the decomposed, discretized, time-stepping equation.

The pseudo-time stepping equation is thus expressed in the form

$$\left( \hat{\Theta} \mathbf{I} + \frac{\partial \hat{\mathbf{r}}}{\partial \mathbf{u}} \Big|_{\mathbf{u}=\mathbf{u}_J} \right) \Delta \mathbf{u}_J^n = \mathbf{D}_J \Delta \mathbf{u}_J^n - \mathbf{M}_{J-1}^+ \Delta \mathbf{u}_{J-1}^n + \mathbf{M}_{J+1}^- \Delta \mathbf{u}_{J+1}^n = -\hat{\mathbf{r}}_J^n, \quad (5.13)$$

where the  $\mathbf{D}$  submatrix contains the diagonal elements of the original matrix, and the  $\mathbf{M}^+$  and  $\mathbf{M}^-$  submatrices contain the off-diagonal elements in the negative and positive computational coordinate directions, respectively. Based on the flux difference splitting scheme given in (5.12), these matrices are given by

$$\begin{aligned} \mathbf{D}_J &= (\hat{\Theta} + i\omega \bar{\nu}) \mathbf{I} - \bar{\nu} \frac{\partial \mathbf{S}}{\partial \mathbf{U}} \Big|_{\mathbf{U}=\mathbf{U}_J} + \left( \frac{\partial \hat{\mathbf{F}}}{\partial \mathbf{U}} \right)_{J,J+1/2} - \left( \frac{\partial \hat{\mathbf{F}}}{\partial \mathbf{U}} \Big|_{\mathbf{U}=\mathbf{U}_{J+1/2}^{\text{Roe}}} \right)^- - \left( \frac{\partial \hat{\mathbf{F}}}{\partial \mathbf{U}} \Big|_{\mathbf{U}=\mathbf{U}_{J-1/2}^{\text{Roe}}} \right)^- \\ \mathbf{M}_{J-1}^+ &= \left( \frac{\partial \hat{\mathbf{F}}}{\partial \mathbf{U}} \right)_{J-1,J-1/2} - \left( \frac{\partial \hat{\mathbf{F}}}{\partial \mathbf{U}} \Big|_{\mathbf{U}=\mathbf{U}_{J-1/2}^{\text{Roe}}} \right)^- \quad \text{and} \quad \mathbf{M}_{J+1}^- = \left( \frac{\partial \hat{\mathbf{F}}}{\partial \mathbf{U}} \Big|_{\mathbf{U}=\mathbf{U}_{J+1/2}^{\text{Roe}}} \right)^-, \end{aligned} \quad (5.14)$$

where the  $J$  subscript refers to the  $J$ th cell, the  $J \pm 1/2$  subscripts refer to the right and left interfaces of this cell, and  $J - 1$  refers to the adjacent upstream cell.

Introducing  $l$  as the Gauss-Seidel iteration index, the iteration formula for the linearized unsteady equation has the form

$$\mathbf{D}_J \Delta \mathbf{u}_J^* - \mathbf{M}_{J-1}^+ \Delta \mathbf{u}_{J-1}^* = -\mathbf{M}_{J+1}^- \Delta \mathbf{u}_{J+1}^{l-1} - \mathbf{r}_J^n \quad (5.15)$$

$$\mathbf{D}_J \Delta \mathbf{u}_J^l + \mathbf{M}_{J+1}^- \Delta \mathbf{u}_{J+1}^l = \mathbf{M}_{J-1}^+ \Delta \mathbf{u}_{J-1}^* - \mathbf{r}_J^n ,$$

where  $l = 1, 2, \dots, L$ ,  $\mathbf{u}_J^0 = \mathbf{u}_J^n$ ,  $\Delta \mathbf{u}_J^* = \mathbf{u}_J^* - \mathbf{u}_J^n$ ,  $\Delta \mathbf{u}_J^l = \mathbf{u}_J^l - \mathbf{u}_J^n$ , and  $\mathbf{u}_J^L \approx \mathbf{u}_J^{n+1}$ . The first SGS iteration is over negative grid indices and the second iteration is over positive grid indices. The iteration procedure is thus an  $LU$  decomposition of the pseudo-time update matrix, with forward and backward substitution. Once the pseudo-time solutions converge to a steady state, i.e.,  $\|\hat{\mathbf{r}}\| \rightarrow 0$ , any error introduced by the iteration scheme (5.15) vanishes. Only the discretization errors in the residual calculation of equation (5.1) remain. The current LINFLUX implementation uses explicit boundary conditions, which are incorporated into the LU-SGS iteration procedure, so that the boundary conditions are imposed in a semi-implicit manner. This boundary condition treatment has been found to yield better convergence properties than a purely explicit implementation.

## 6. Numerical Results

Unsteady aerodynamic response predictions will be presented for three-dimensional flows through a flat-plate stator and a real-blade rotor based on the Tenth Standard Cascade Configuration [FV93], to demonstrate the current status of the LINFLUX code. In each case, the blade row consists of 24 airfoils, operates within a cylindrical annular duct with an inner radius  $r_H = 3.39$  and an outer radius  $r_D = 4.24$ , there is no clearance between the blades and the outer duct wall, and the steady background flow at inlet is uniform relative to a space-fixed or inertial reference frame.

We will consider unsteady flows that are excited by prescribed single-degree-of-freedom (SDOF), harmonic, blade motions (see Figure 6.1). The latter occur at unit frequency ( $\omega = 1$ ) and with constant phase angle  $\sigma$  between the motions of adjacent blades. The blade motions to be considered are pure translations normal to the blade chords (bending) and pure rotations about axes at the blade midchords (torsion). These motions [see (2.1)] are defined by  $\mathbf{R}_B = h\mathbf{e}_n$  and  $\mathbf{R}_B(\bar{\mathbf{x}}_B) = \boldsymbol{\alpha} \times (\bar{\mathbf{x}}_B - \bar{\mathbf{x}}_P)$ , respectively, where  $h$  and  $\boldsymbol{\alpha}$  are the complex amplitudes of the bending and torsional vibrations,  $\mathbf{n}$  is a unit normal to the blade chord plane, and  $\bar{\mathbf{x}}_B - \bar{\mathbf{x}}_P$  is the distance between a point,  $\bar{\mathbf{x}}_B$ , on the mean reference blade surface and the point,  $\bar{\mathbf{x}}_P$ , at the same radius, on the mean position of the torsional axis. To allow a convenient comparison between LINFLUX predictions and those of two-dimensional unsteady flow codes, we have assumed that the complex amplitudes of the vibratory blade motions are constant along the span. In addition to the flows excited by blade vibration, we will also consider an unsteady flow through the rotor blade row that is excited by an acoustic plane wave that travels through the duct in the axial flow direction.

In addition to the LINFLUX results given below, for purposes of comparison, we will present nonlinear response predictions based on the TURBO analysis, and linear response predictions based on the two-dimensional classical analysis of Smith [Smi72] and on the two-dimensional LINFLO analysis [Ver93]. In the Smith analysis, the unsteady flow is regarded as a small perturbation of uniform stream; in LINFLO, as a small perturbation of a nonlinear potential steady background flow. The TURBO analysis has been used to provide the steady background flow information for the LINFLUX real blade calculations. The steady full-potential analysis CASPOF [Cas83] has been used to provide this information for the LINFLO calculations. Accurate far-field conditions have not yet been incorporated into the TURBO or LINFLUX codes; therefore, at present, these analyses can only be applied to flows excited by blade vibrations or external aerodynamic disturbances that travel axially.

The TURBO nonlinear steady and unsteady solutions and the LINFLUX linearized unsteady solutions have been determined on H-type meshes. The grid generated with the TIGER grid generator [SS91] for the subsonic calculations, reported below, consists of 141 axial, 41 tangential and 9 radial surfaces (44,800 cells). For the flows excited by blade motions, this grid was stretched axially and extended to 5 axial chords upstream and to 9 axial chords downstream from the blade row to dissipate oblique outgoing waves. For the rotor flow excited by the planar acoustic excitation, the mesh extended two axial chords upstream and one axial chord downstream of the blade row. The axial grid distribution is clustered near blade leading and trailing edges, the circumferential grid distribution is clustered near blade surfaces, and the radial grid distribution is uniform.

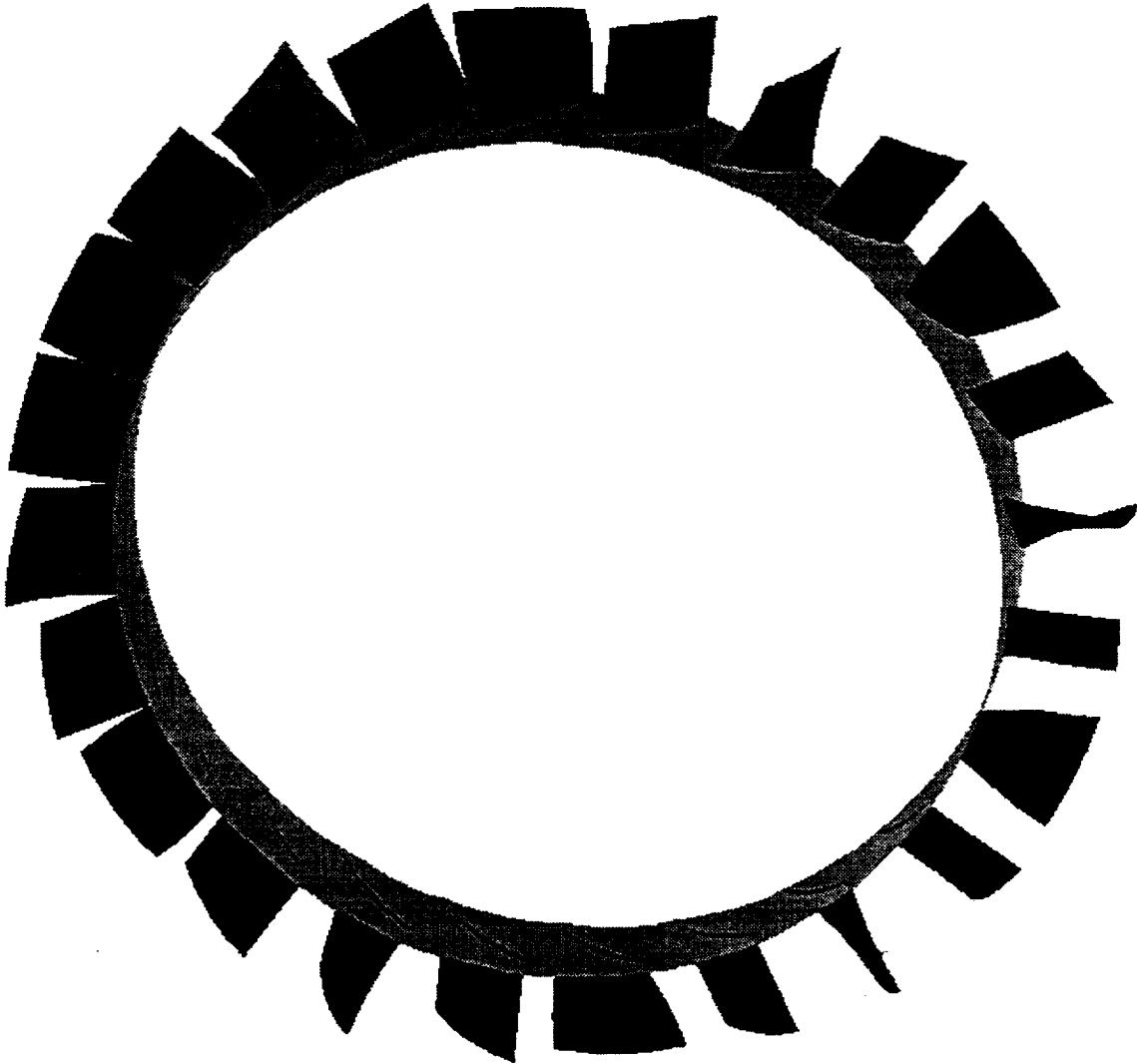


Figure 6.1: 3D Tenth Standard Configuration undergoing an exaggerated torsional motion ( $\alpha_{hub} = 0$  deg,  $\alpha_{tip} = 45$  deg). The rotor consists of 24 NACA 5506 airfoils staggered at 45 deg. The nodal diameter of the blade motion is 6, which results in an interblade phase angle of 90 deg. The outer casing has been eliminated from the figure for clarity.

The full potential steady and the LINFLO linearized unsteady solutions were determined on composite meshes consisting of local C-meshes embedded in global H-meshes. The H- and C-meshes used with LINFLO consisted of 155 axial and 41 tangential lines and 101 radial and 21 circumferential lines, respectively. Coarser meshes were used for the CASPOF calculations. Since analytic, two-dimensional, far-field conditions are applied, the H-meshes extended only one axial chord upstream and downstream from the blade row.

The numerical solutions reported herein were determined on an IBM-390 Workstation.

The TURBO steady subsonic solutions required 13 CPU hours. The TURBO unsteady calculations were started from the appropriate steady solution and required 18 CPU hours per blade passage. The number of blade passages included in a nonlinear unsteady calculation depends upon the interblade phase angle. For example, if  $\sigma = 60$  deg, six passages are needed. The TURBO calculations were performed using 500 time-steps per cycle of unsteady motion, 4 iterative refinements, involving Newton and symmetric Gauss-Siedel iterations, per time step, and three cycles of motion were used to converge the nonlinear inviscid solutions to a periodic state. The LINFLUX linearized unsteady calculations required 2 1/2 CPU hours. They were performed using 2000 pseudo time steps and 2 SGS iterations per pseudo time step.

## 6.1 Flat-Plate Stator

The flat plate stator consists of 24 unstaggered blades. The inlet flow is axial and uniform, with  $M_{\text{abs},-\infty} = M_{\text{rel},-\infty} = 0.5$ , where the subscripts refer to the absolute and relative inlet freestream conditions. This geometry and flow condition were chosen as a first LINFLUX test case both because of its simplicity and to allow meaningful comparisons of LINFLUX predictions with those of the two-dimensional, semi-analytic analysis of Smith [Smi72].

The 3D LINFLUX and the 2D Smith analyses were applied to predict unsteady flows produced by SDOF bending and torsional blade vibrations. These motions occur at unit amplitude, at unit reduced frequency, and at interblade phase angles,  $\sigma = 360$  ND/N deg, ranging from 0 to 180 deg in increments of 15 deg, i.e.,  $ND = 0, 1, 2, \dots, 12$ . Results for in- ( $\sigma = 0$  deg) and out-of-phase ( $\sigma = 180$  deg) blade motions are shown in Figure 6.2, where the LINFLUX and semi-analytic predictions are given for the real (in-phase with blade displacement) and imaginary (out-of-phase with blade displacement) components of the unsteady pressure jump across a blade surface,  $[[p]] = p_{\text{lower}} - p_{\text{upper}}$ , at midspan ( $r/r_D = 0.9$ ). The results of the two analyses are in excellent agreement for the in-phase blade motions, in good agreement for the out-of-phase torsional vibration; but, they are in poor agreement for the out-of-phase bending motion.

The predictions for the unsteady pressure jumps across the flat-plate blades undergoing torsional blade vibrations at  $\sigma = 15$  ND deg,  $ND = 0, 1, 2, \dots, 12$ , indicate that the LINFLUX and Smith results are in good agreement over this range of interblade phase angles. However, the corresponding predictions for bending vibrations are in good agreement only for low values of  $\sigma$ . We have conducted a detailed investigation of the LINFLUX solutions for the bending motions and a careful examination of the LINFLUX coding. At this point, we have not uncovered the cause for the discrepancies between the LINFLUX and the semi-analytic results. As a result, we will continue to address this issue in our future work.

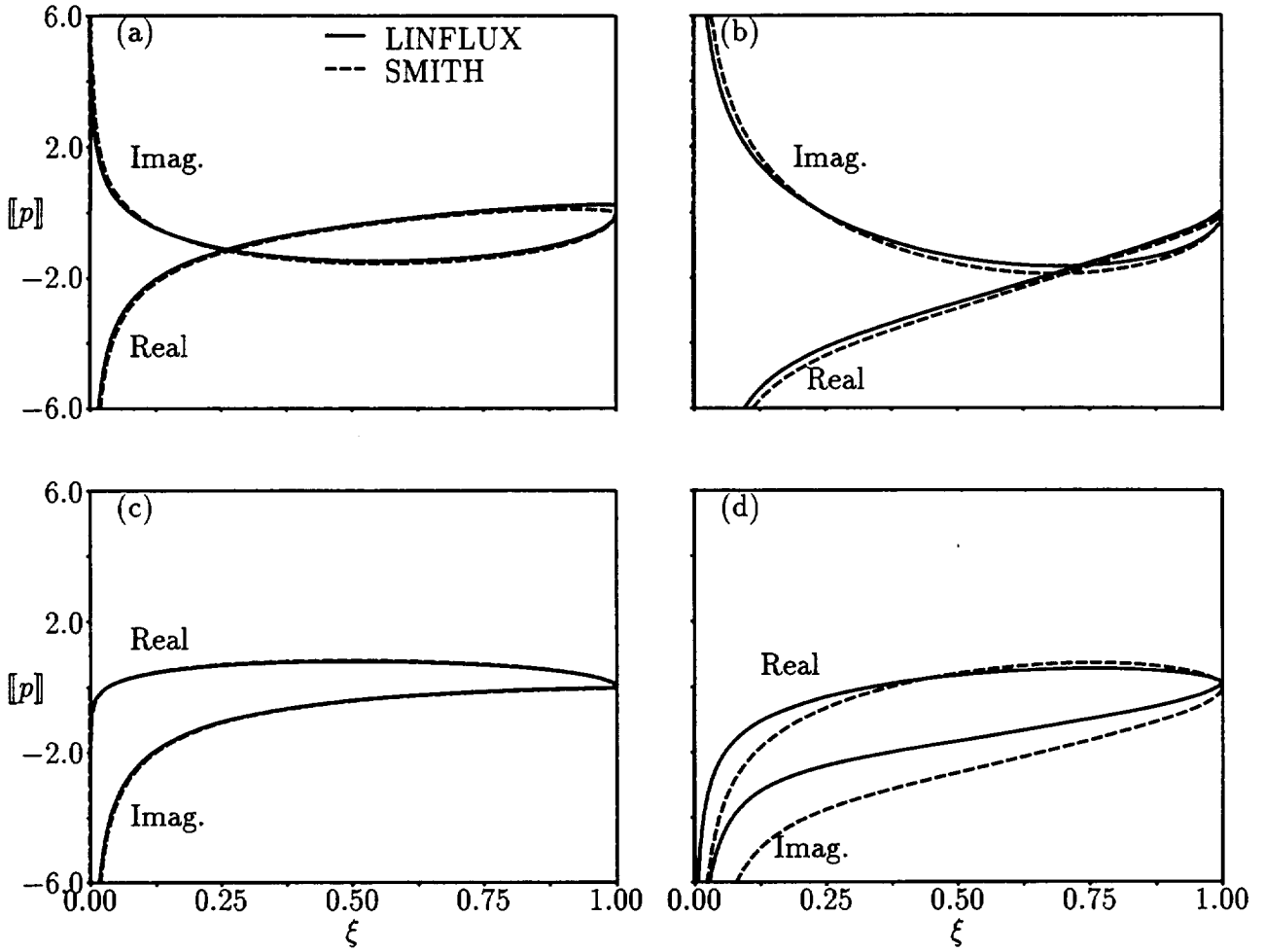


Figure 6.2: Unsteady pressure difference distributions, as predicted by the 3D LINFLUX and the 2D Smith analyses, at mid-span of the flat-plate stator with blades vibrating at unit amplitude and unit reduced frequency: (a) torsion about midchord at  $\sigma = 0$  deg, (b) torsion about midchord at  $\sigma = 180$  deg, (c) bending at  $\sigma = 0$  deg, (d) bending at  $\sigma = 180$  deg.

## 6.2 3D Tenth Standard Configuration

This rotor consists of 24 NACA 5506 airfoils staggered at an angle,  $\Theta$ , of 45 deg (see Figure 6.1). The absolute inlet Mach number  $M_{\text{abs},-\infty}$  is 0.402 and the rotational speed is  $|\Omega| = 0.214$ . This geometry and flow condition were chosen to match the subsonic Tenth Standard Configuration at mid span, i.e.,  $M_{\text{rel},-\infty} = 0.7$ ,  $\Omega_{\text{rel},-\infty} = 55$  deg and  $G = 1.0$  at  $r/r_D = 0.9$ , where  $M_{\text{rel},-\infty}$  and  $\Omega_{\text{rel},-\infty}$  are the relative inlet Mach number and flow angle, and  $G$  is the circumferential blade spacing. The steady, surface, Mach number distributions predicted by the TURBO and CASPOF (at  $r/r_D = 0.9$ ) analyses are shown in Figure 6.3.

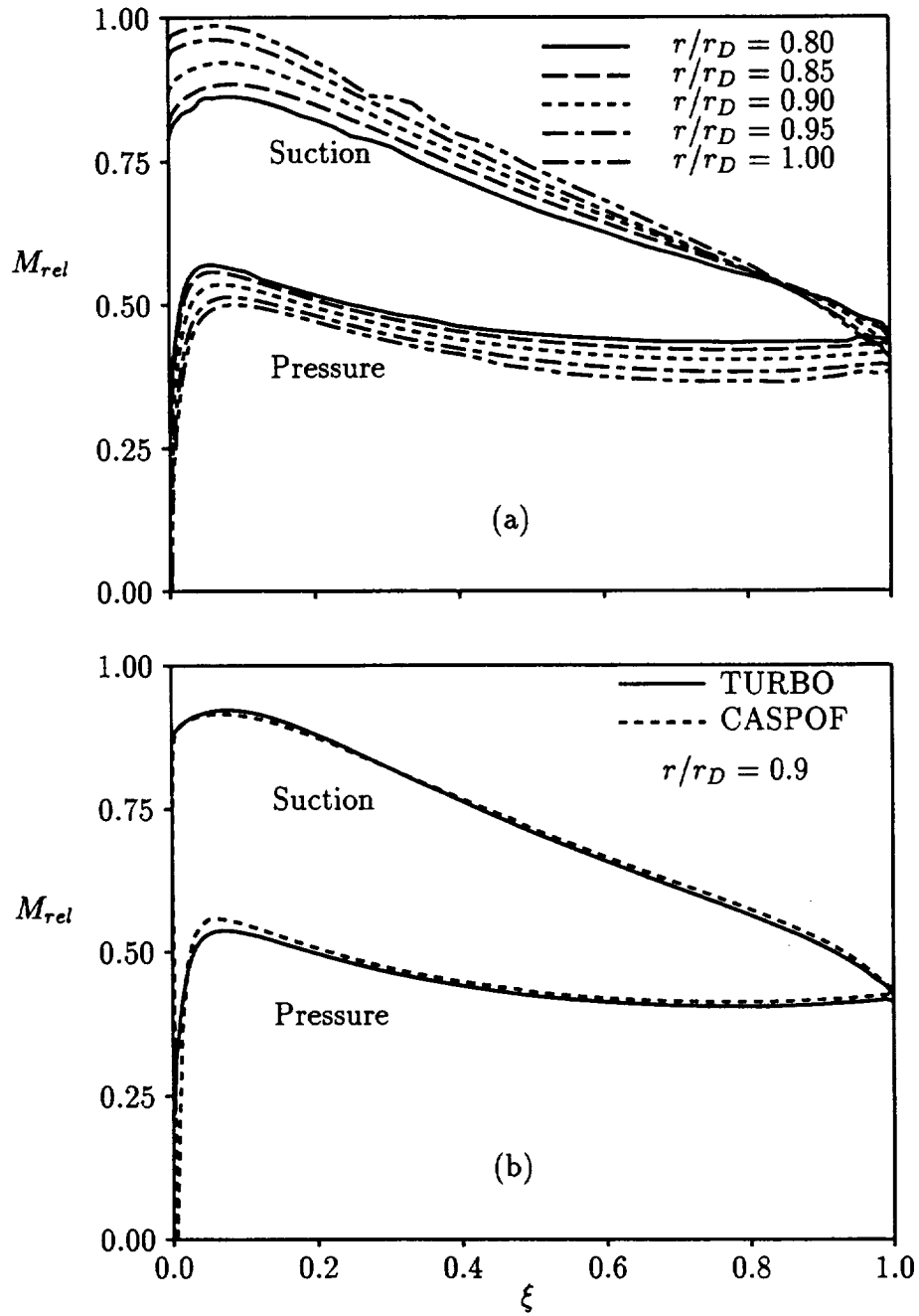


Figure 6.3: Relative surface Mach number distributions for the Tenth Standard Configuration ( $M_{abs,-\infty} = 0.402$ ,  $|\Omega| = 0.214$ ): (a) TURBO predictions; (b) TURBO and CASPOF predictions at midspan.

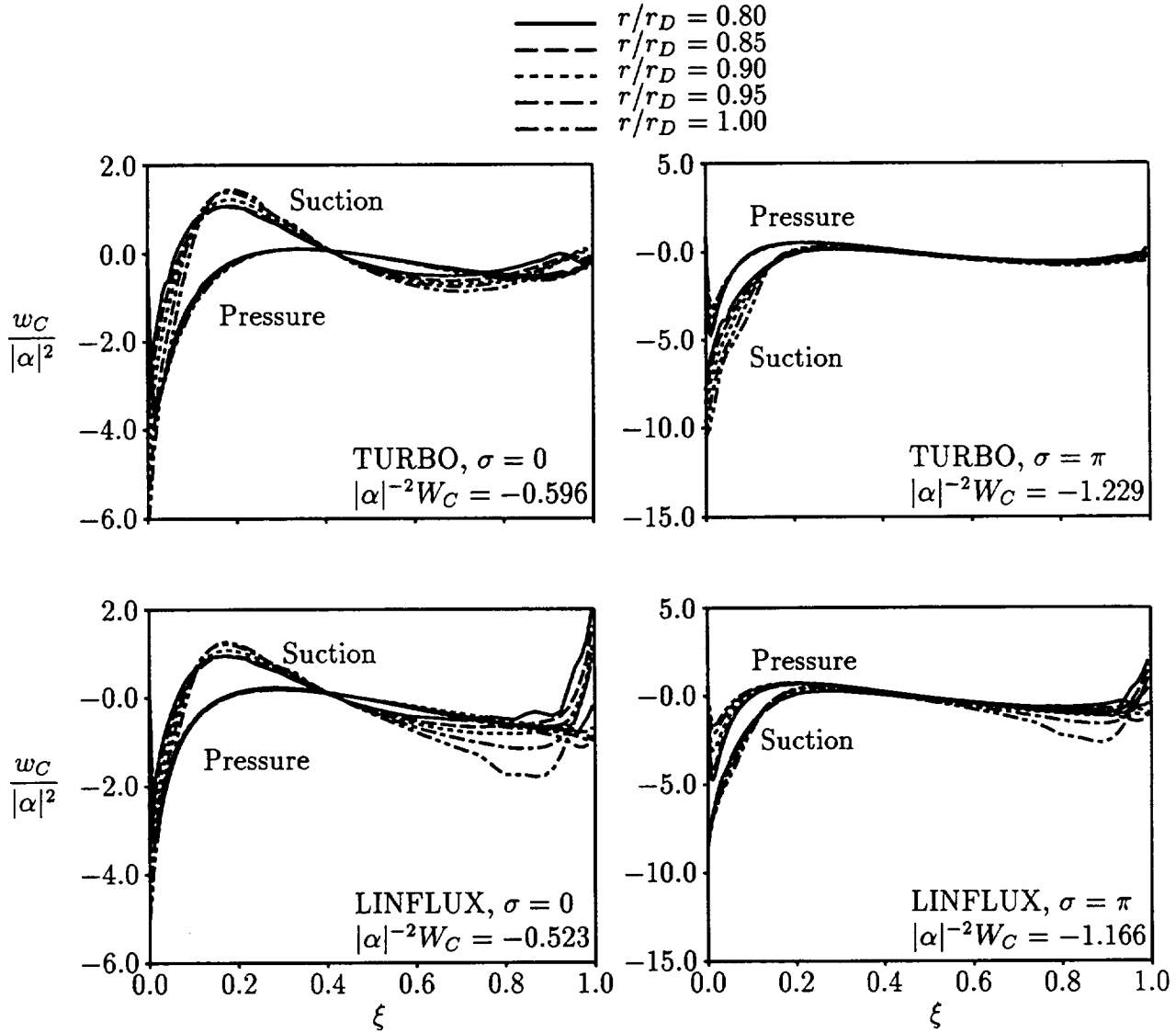


Figure 6.4: Local work per cycle distributions and global works per cycle, as predicted by the 3D LINFLUX and TURBO analyses, for the subsonic Tenth Standard Configuration with blades undergoing in- and out-of-phase torsional vibrations about midchord at a reduced frequency  $\omega = 1$ .

### Blade Vibration

The linearized (LINFLUX) and nonlinear (TURBO) analyses were applied to predict the local ( $w_C$ ) and global ( $W_C$ ) work per cycle responses to blades vibrating in torsion about midchord with an amplitude,  $|\alpha|$ , of 1 degree along the entire span, a reduced frequency,  $\omega$ , of 1.0, and interblade phase angles,  $\sigma$ , of 0 deg and 180 deg. The local and global works per cycle are given by

$$w_C(\bar{x}_B) = -\omega^{-1} \int_{\phi}^{\phi+2\pi} \tilde{P}_B \frac{\partial \mathcal{R}_B}{\partial t} \cdot \frac{d\mathbf{A}_B}{|d\mathbf{A}_B|} d(\omega t) \quad \text{and} \quad W_C = \int_{A_B} w_C(\bar{x}) dA_B, \quad (6.1)$$

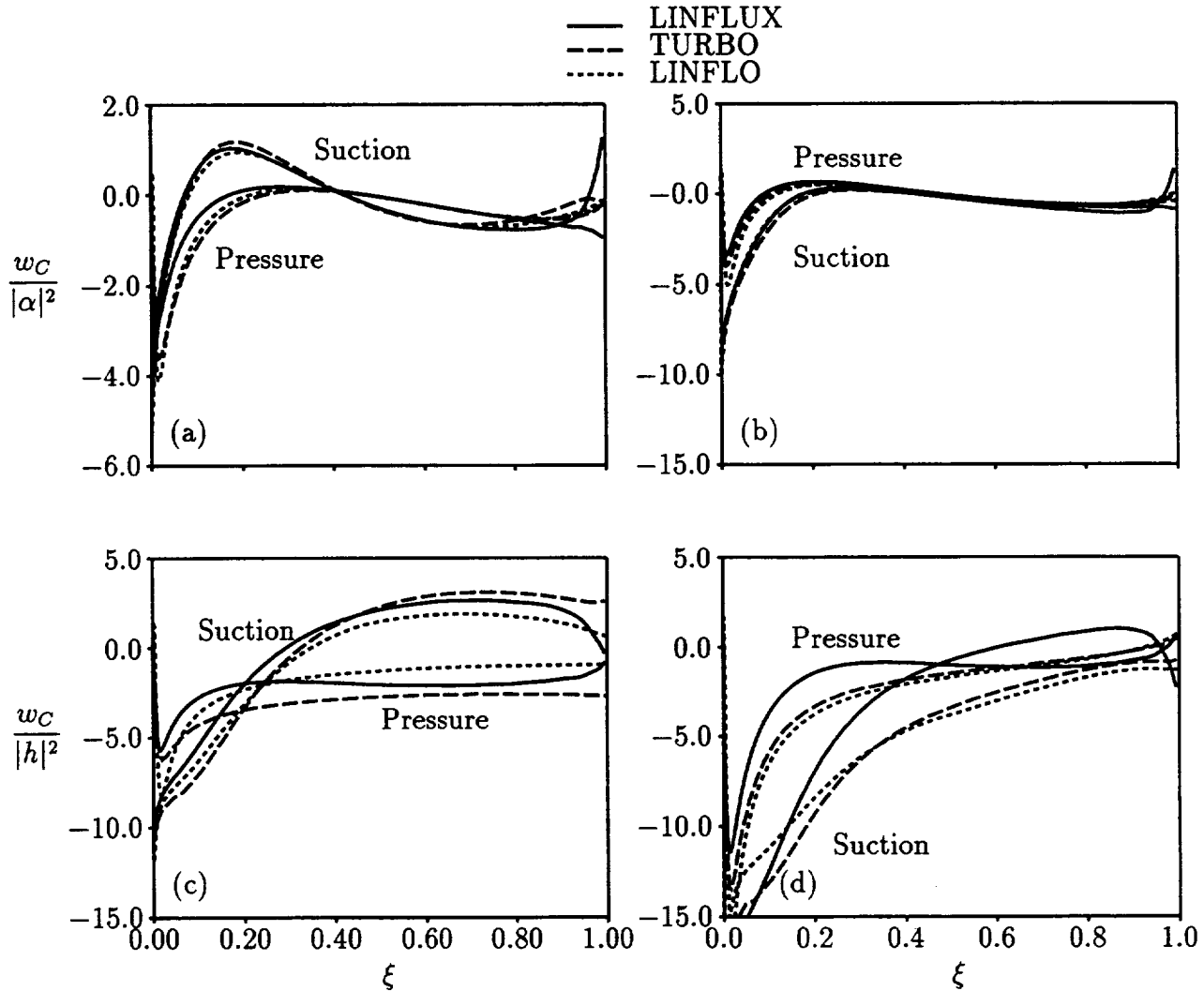


Figure 6.5: Local work per cycle distributions at blade midspan, as predicted by the 3D LINFLUX and TURBO analyses and the 2D LINFLO analysis, for the subsonic 3D Tenth Standard Configuration with blades oscillating at unit reduced frequency: (a) torsion about midchord,  $\sigma = 0$  deg; (b) torsion about midchord,  $\sigma = 180$  deg; (c) bending,  $\sigma = 0$  deg; (d) bending,  $\sigma = 180$  deg.

where the subscripts  $\mathcal{B}$  and  $\mathcal{B}$  refer to the instantaneous and the mean blade surfaces, respectively, and  $d\mathcal{A}$  is a directed differential surface area. For small amplitude blade motions

$$w_C(\bar{x}_{\mathcal{B}}) \approx -\pi \text{Im}\{(P d\mathcal{A}_{\mathcal{B}} + p d\mathcal{A}_{\mathcal{B}}) \cdot \mathbf{R}_{\mathcal{B}}^* / |d\mathcal{A}_{\mathcal{B}}|\}, \quad (6.2)$$

where  $\text{Im}\{ \}$  denotes the imaginary part of  $\{ \}$  and  $d\mathcal{A}_{\mathcal{B}} \approx d\mathcal{A}_{\mathcal{B}} - d\mathcal{A}_{\mathcal{B}}$ .

The results are shown in Figure 6.4 where the local work per cycle responses are given for  $r/r_D = 0.8, 0.85, 0.9, 0.95$  and  $1.0$ . The TURBO and LINFLUX predictions are generally in good agreement, except for those on the suction surface, at the outer span of the blade, from

approximately 70% of axial chord to the trailing edge. The LINFLUX and TURBO predictions should be nearly identical, since LINFLUX is a derivative of TURBO and nonlinear effects should be small for the motions considered. The differences between the nonlinear and linear results in Figure 6.4 are probably due to the sensitivity of the linearized analysis to any errors that are present in the nonlinear solution for the steady background flow near blade surfaces, where numerical losses tend to be high and grow with distance along the blades. Similar errors were present in 2D LINFLUX predictions [VMK95, MV95], and were reduced by decreasing the normal grid spacing near a blade surface. Steady predictions can often be improved by altering the computational mesh, but a better solution would be to implement more accurate approximations of the surface boundary-conditions into both the TURBO and LINFLUX analyses.

LINFLUX, TURBO, and 2D LINFLO predictions for the local work per cycle responses at midspan, to blades undergoing pure torsional vibrations about their midchords and pure bending vibrations, are shown in Figure 6.5 for  $\sigma = 0$  deg and  $\sigma = 180$  deg. The torsional and bending amplitudes are constant along the entire span and were set at 1 deg and at 1% of blade chord, respectively, for the nonlinear calculation. The various response predictions for the in- and out-of-phase torsional vibrations are in reasonably good agreement, except for the LINFLUX predictions near the blade trailing edge. The results for in-phase bending show similar qualitative behaviors, but significant quantitative differences over the entire blade. The TURBO and LINFLO results for out-of-phase bending are in fair agreement, but the LINFLUX results differ substantially from those of the other analyses. This is consistent with the behavior observed for the flat-plate stator predictions.

### *Acoustic Excitation*

As a final example, we consider the interaction of an acoustic plane wave that travels in the axial direction with the subsonic 3D Tenth Standard Cascade. The acoustic disturbance occurs at unit amplitude with  $p_{I,-\infty} = (1,0)$ , unit frequency and zero interblade phase angle. The results of the 3D LINFLUX analysis for the unsteady surface pressures acting on each blade and those of the LINFLUX and the 2D LINFLO analyses for the unsteady surface pressures acting at blade midspan,  $r/r_D = 0.9$ , are shown in Figures 6.6 and 6.7, respectively. The LINFLUX results in Figure 6.6 show a reasonable variation with radius, and those in Figure 6.7 are in good agreement with the LINFLO predictions. Contours of the in-phase component of the unsteady pressure at  $r/r_D = 0.9$ , as predicted by the LINFLUX and LINFLO analyses, are shown in Figure 6.8. Again the results of the two analyses are seen to be in good agreement. We should note that, because of three-dimensional effects, the LINFLUX and LINFLO results are not expected to be in perfect agreement for the 3D Tenth Standard Configuration, even for the simple flows considered in this report.

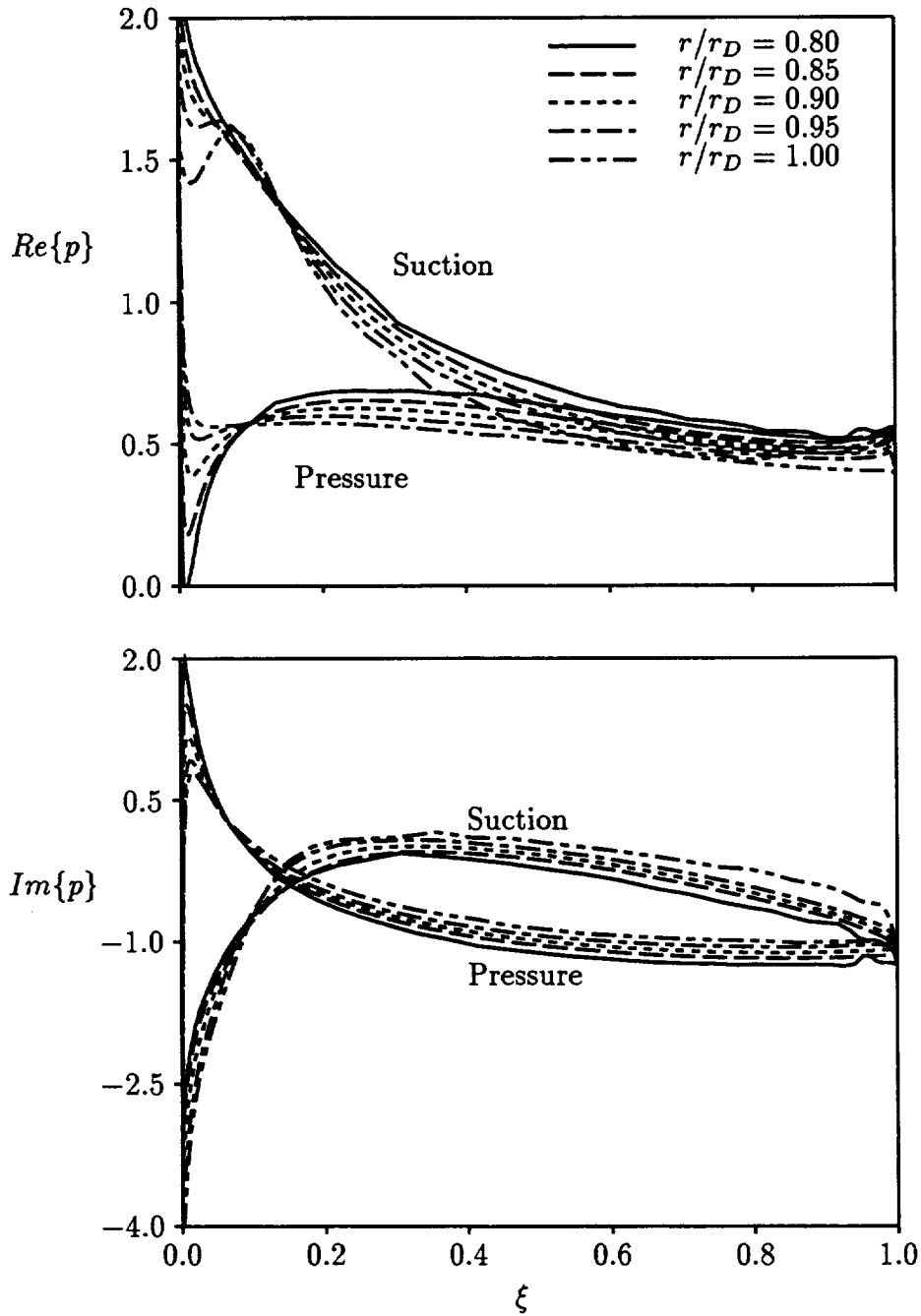


Figure 6.6: Unsteady surface pressure distributions, as predicted by the 3D LINFLUX analysis, due to the interaction between an acoustic excitation from upstream, with  $p_{I,-\infty} = (1, 0)$ ,  $\omega = 1$ , and  $\sigma = 0$  deg, and the subsonic 3D Tenth Standard Configuration.

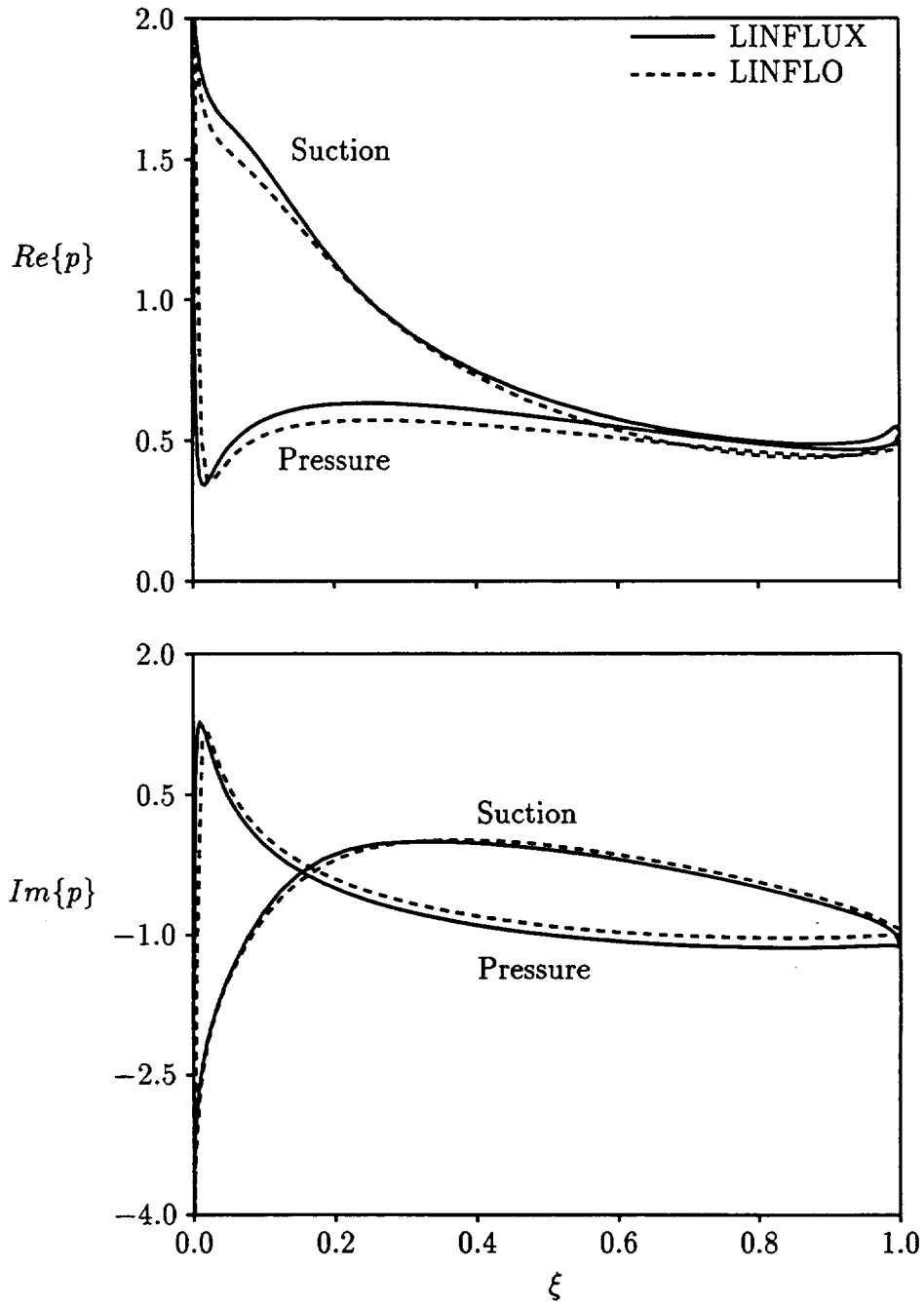


Figure 6.7: Unsteady surface pressure distributions at midspan, as predicted by the 3D LINFLUX and the 2D LINFLO analyses, due to the interaction between an acoustic disturbance from upstream, with  $p_{I,-\infty} = (1, 0)$ ,  $\omega = 1$ , and  $\sigma = 0$  deg, and the subsonic 3D Tenth Standard Configuration.

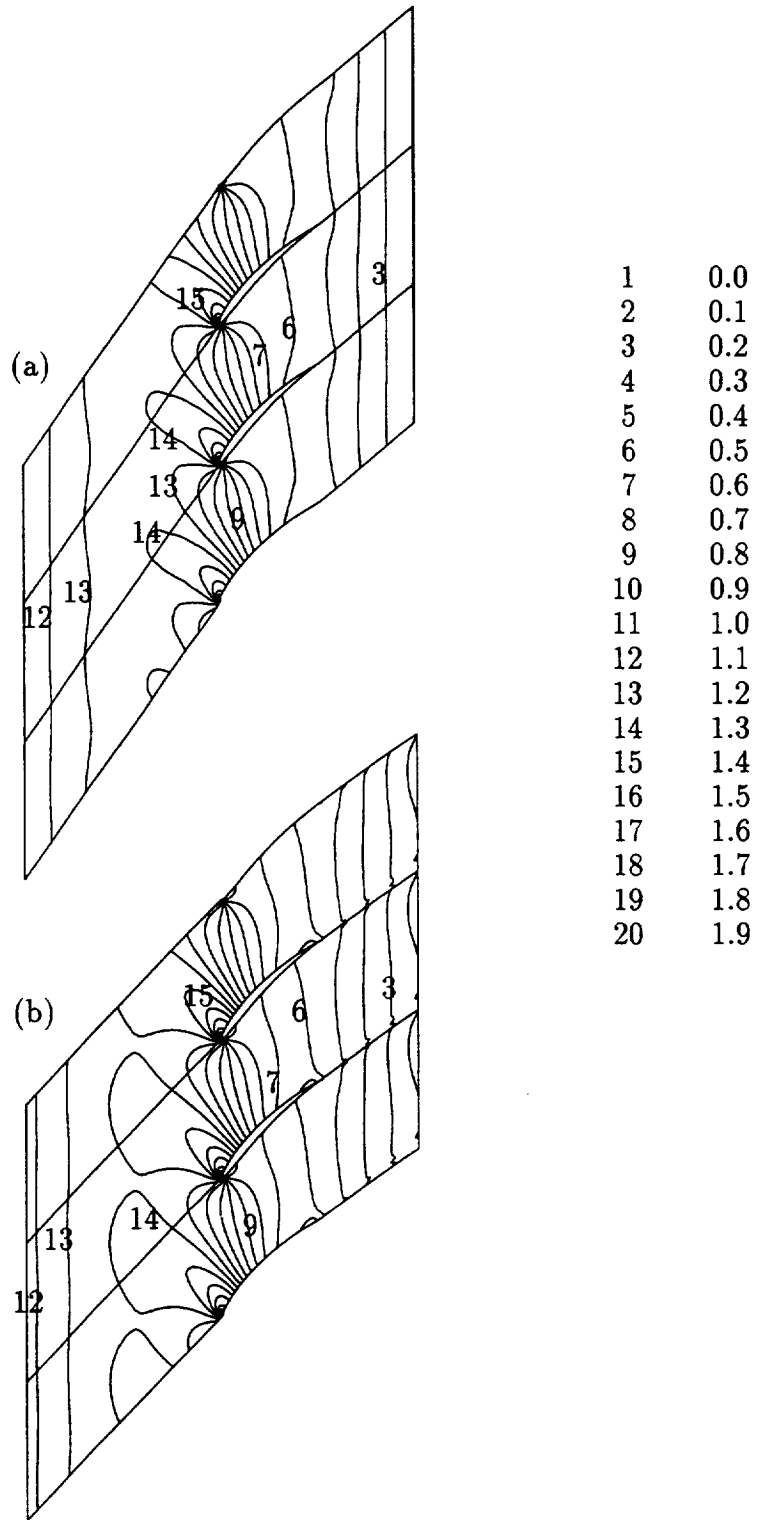


Figure 6.8: Contours of the in-phase component of the unsteady pressure at midspan ( $r/r_D = 0.9$ ) due to the interaction between an acoustic disturbance from upstream, with  $p_{I,-\infty} = (1,0)$ ,  $\omega = 1$ , and  $\sigma = 0$  deg, and the subsonic 3D Tenth Standard Configuration: (a) LINFLO calculation; (b) LINFLUX calculation.

## 7. Concluding Remarks

A linearized unsteady aerodynamic analysis is being developed for turbomachinery aeroelastic and aeroacoustic design applications. This analysis, called LINFLUX, is based on the Euler equations of fluid motion and the implicit, flux-split, finite-volume scheme used in the nonlinear unsteady analysis, TURBO [JHW92]. To date, the effort has been focused on formulating the linearized inviscid unsteady aerodynamic and numerical models and on implementing these models, first, into a two-dimensional code, and then into a three-dimensional code. The two-dimensional analysis and its application to unsteady subsonic and transonic flows is described in [VMK95, MV95]. The first applications of the 3D LINFLUX analysis to very simple, benchmark, unsteady flows have been described in this report.

We have applied the 3D LINFLUX analysis to unsteady subsonic flows through a flat plate stator and a “real” blade rotor, which is a three dimensional version of the 10th Standard Cascade Configuration. The unsteady flows are excited by prescribed blade vibrations, and, in one example, an acoustic plane wave that travels in the axial flow direction. In each case, the LINFLUX predictions have been compared with predictions based on previous analyses. The results of this study indicate that the current version of the 3D LINFLUX analysis gives accurate aerodynamic response information for unsteady subsonic flows excited by torsional blade vibrations, in-phase bending vibrations, and planar acoustic excitations. However, there is an error in the existing code (cf. Figures 6.2d and 6.5d) that must be located and corrected before reliable response predictions can be determined for flows excited by bending vibrations at non-zero interblade phase angles. Additional work is also needed (cf. Figure 6.5) to ensure that the TURBO and LINFLUX analyses give nearly identical response predictions for unsteady flows driven by small-amplitude excitations.

Based upon our earlier 2D work, we also note that improvements will be needed in the LINFLUX analyses to accurately predict unsteady transonic flows and unsteady flows excited by vortical gusts. In particular, the shock modeling used in LINFLUX must be improved, so that LINFLUX and its nonlinear counterpart, TURBO, provide consistent response information in the vicinities of shocks. Also, the surface boundary conditions used in both codes should be improved to reduce numerical losses and to allow more accurate descriptions of unsteady vortical behaviors near blade surfaces. The latter may require the implementation of higher-order surface boundary conditions into the nonlinear and linearized codes.

The TURBO and LINFLUX analyses are being developed to provide useful nonlinear and linearized unsteady aerodynamic analyses for three-dimensional flows in which the effects of radial flow and mean swirl are important. For this purpose, accurate far-field conditions must be implemented. Thus, in a follow-on effort, work will be directed towards establishing and implementing appropriate far-field conditions for three-dimensional unsteady flows. Such conditions will preclude the need for using axially-stretched meshes in blade flutter calculations and allow the consideration of unsteady flows excited by arbitrary external aerodynamic excitations. The 3D LINFLUX code development effort is being continued under Contract NAS3-26618, where the emphasis is being placed on predicting the aeroacoustic responses of blade rows to external aerodynamic excitations. Work to improve the current flutter prediction capabilities of LINFLUX will also continue under this Contract.

## References

- [AV94] T. C. Ayer and J. M. Verdon. Numerical Unsteady Aerodynamic Simulator for Blade Forced Response Phenomena. Contractor Report WL-TR-95-2011, prepared for the GUIde Consortium under U. S. Air Force Contract F33615-92-C-2212, December 1994.
- [Cas83] J. R. Caspar. Unconditionally Stable Calculation of Transonic Potential Flow through Cascades using an Adaptive Mesh for Shock Capture. *Transactions of the ASME: Journal of Engineering for Power*, 105(3):504-513, July 1983.
- [FV93] T. H. Fransson and J. M. Verdon. Standard Configurations for Unsteady Flow through Vibrating Axial-Flow Turbomachine Cascades. In *Unsteady Aerodynamics, Aeroacoustics and Aeroelasticity of Turbomachines and Propellers*, pages 859-889. Edited by H. M. Atassi, Springer-Verlag, New York, 1993.
- [Gil93] M. B. Giles. A Framework for Multi-Stage Unsteady Flow Calculations. In *Unsteady Aerodynamics, Aeroacoustics, and Aeroelasticity of Turbomachines and Propellers*, pages 57-72. Edited by H. M. Atassi, Springer-Verlag, New York, 1993.
- [HC93a] K. C. Hall and W. S. Clark. Linearized Euler Predictions of Unsteady Aerodynamic Loads in Cascades. *AIAA Journal*, 31(3):540-550, March 1993.
- [HC93b] D. G. Holmes and H. A. Chuang. 2D Linearized Harmonic Euler Flow Analysis for Flutter and Forced Response. In *Unsteady Aerodynamics, Aeroacoustics, and Aeroelasticity of Turbomachines and Propellers*, pages 213-230. Edited by H. M. Atassi, Springer-Verlag, New York, 1993.
- [HCL93] K. C. Hall, W. S. Clark, and C. B. Lorence. A Linearized Euler Analysis of Unsteady Transonic Flows in Turbomachinery. ASME Paper 93-GT-94, 38th International Gas Turbine and Aeroengine Congress and Exposition, Cincinnati, Ohio, May 24-27 1993.
- [HL92] K. C. Hall and C. B. Lorence. Calculation of Three-Dimensional Unsteady Flows in Turbomachinery Using the Linearized Harmonic Euler Equations. ASME Paper 92-GT-736, International Gas Turbine and Aeroengine Congress and Exposition, Cologne, Germany, June 1-4 1992.
- [HSR91] D. L. Huff, T. W. Swafford, and T. S. R. Reddy. Euler Flow Predictions for an Oscillating Cascade Using a High Resolution Wave-Split Scheme. ASME Paper 91-GT-198, International Gas Turbine and Aeroengine Congress and Exposition, Orlando, Florida, June 3-6 1991.
- [JHW92] J. M. Janus, H. Z. Horstman, and D. L. Whitfield. Unsteady Flowfield Simulation of Ducted Prop-fan Configurations. Paper 92-0521, AIAA 30th Aerospace Sciences Meeting and Exhibit, Reno, Nevada, January 6-9 1992.

- [KK93] G. Kahl and A. Klose. Computation of Time Linearized Transonic Flow in Oscillating Cascades. ASME Paper 93-GT-269, 38th International Gas Turbine and Aeroengine Congress and Exposition, Cincinnati, Ohio, May 24-27 1993.
- [MV95] M. D. Montgomery and J. M. Verdon. A Linearized Unsteady Euler Analysis for Turbomachinery Blade Rows Using an Implicit Wave-Split Scheme. In *Unsteady Aerodynamics and Aeroelasticity of Turbomachines*, pages 143-160. Edited by Y. Tanida and M. Namba, Elsevier, Amsterdam, 1995.
- [Nam87] M. Namba. Three Dimensional Flows. In *AGARD Manual on Aeroelasticity in Axial-Flow Turbomachines*, Vol. 1, *Unsteady Turbomachinery Aerodynamics*, chapter IV. Edited by M. F. Platzer and F. O. Carta, AGARD AG-298, March 1987.
- [Roe81] P. L. Roe. Approximate Riemann Solvers, Parameter Vectors and Difference Schemes. *Journal of Computational Physics*, 43:357-372, 1981.
- [SLH+94] T. W. Swafford, D. H. Loe, D. L. Huff, D. H. Huddleston, and T. S. R. Reddy. The Evolution of NPHASE: Euler/Navier-Stokes Computations of Unsteady Two-Dimensional Cascade Flow Fields. AIAA Paper 94-1834, 12th Applied Aerodynamics Conference, Colorado Springs, Colorado, June 20-23 1994.
- [Smi72] S. N. Smith. Discrete Frequency Sound Generation in Axial Flow Turbomachines. R&M 3709, British Aeronautical Research Council, London, England, UK, March 1972.
- [SS91] B. K. Soni and M. H. Shih. Tiger: Turbomachinery Interactive Grid Generation. In *Proceedings of the Third International Conference on Numerical Grid Generation in CFD*, Barcelona, Spain, June 1991.
- [SW81] J. L. Steger and R. F. Warming. Flux Vector Splitting of the Inviscid Gasdynamic Equations with Application to Finite Difference Methods. *Journal of Computational Physics*, 40(2):263-293, April 1981.
- [Ver93] J. M. Verdon. Unsteady Aerodynamic Methods for Turbomachinery Aeroelastic and Aeroacoustic Applications. *AIAA Journal*, 31(2):235-250, February 1993.
- [VMK95] J. M. Verdon, M. D. Montgomery, and K. A. Kousen. Development of a Linearized Unsteady Euler Analysis for Turbomachinery Blade Rows. NASA CR 4677, prepared under Contract NAS3-25425 for NASA Lewis Research Center, June 1995.
- [Whi87] D. S. Whitehead. Classical Two-Dimensional Methods. In *AGARD Manual on Aeroelasticity in Axial-Flow Turbomachines*, Vol. 1, *Unsteady Turbomachinery Aerodynamics*, chapter III. Edited by M. F. Platzer and F. O. Carta, AGARD AG-298, March 1987.

- [WJS88] D.L. Whitfield, J.M. Janus, and L.B. Simpson. Implicit Finite Volume High Resolution Wave Split Scheme for Solving the Unsteady Three-Dimensional Euler and Navier-Stokes Equations on Stationary or Dynamic Grids. Report MSSU-EIRS-ASE-88-2, Mississippi State Engineering and Industrial Research Station, 1988.
- [WT91] D. L. Whitfield and L. Taylor. Discretized Newton-Relaxation Solution of High Resolution Flux-Difference Split Schemes. Paper 91-1539, AIAA 10th Computational Fluid Dynamics Conference, Honolulu, Hawaii, June 24-26 1991.

# REPORT DOCUMENTATION PAGE

Form Approved  
OMB No. 0704-0188

Public reporting burden for this collection of information is estimated to average 1 hour per response, including the time for reviewing instructions, searching existing data sources, gathering and maintaining the data needed, and completing and reviewing the collection of information. Send comments regarding this burden estimate or any other aspect of this collection of information, including suggestions for reducing this burden, to Washington Headquarters Services, Directorate for Information Operations and Reports, 1215 Jefferson Davis Highway, Suite 1204, Arlington, VA 22202-4302, and to the Office of Management and Budget, Paperwork Reduction Project (0704-0188), Washington, DC 20503.

1. AGENCY USE ONLY (Leave blank)	2. REPORT DATE June 1996	3. REPORT TYPE AND DATES COVERED Final Contractor Report	
4. TITLE AND SUBTITLE A Three-Dimensional Linearized Unsteady Euler Analysis for Turbomachinery Blade Rows		5. FUNDING NUMBERS WU-505-62-10 C-NAS3-25425	
6. AUTHOR(S) Matthew D. Montgomery and Joseph M. Verdon		8. PERFORMING ORGANIZATION REPORT NUMBER E-10299	
7. PERFORMING ORGANIZATION NAME(S) AND ADDRESS(ES) United Technologies Research Center Theoretical & Computational Fluid Dynamics Silver Lane East Hartford, Connecticut 06108		10. SPONSORING/MONITORING AGENCY REPORT NUMBER NASA CR-198494 R95-5.101.0003-3	
9. SPONSORING/MONITORING AGENCY NAME(S) AND ADDRESS(ES) National Aeronautics and Space Administration Lewis Research Center Cleveland, Ohio 44135-3191		11. SUPPLEMENTARY NOTES Project Manager, George Stefko, Structures Division, NASA Lewis Research Center, organization code 5230, (216) 433-3920.	
12a. DISTRIBUTION/AVAILABILITY STATEMENT Unclassified - Unlimited Subject Category 02  This publication is available from the NASA Center for AeroSpace Information, (301) 621-0390.		12b. DISTRIBUTION CODE	
13. ABSTRACT (Maximum 200 words)  A three-dimensional, linearized, Euler analysis is being developed to provide an efficient unsteady aerodynamic analysis that can be used to predict the aeroelastic and aeroacoustic response characteristics of axial-flow turbomachinery blading. The field equations and boundary conditions needed to describe nonlinear and linearized inviscid unsteady flows through a blade row operating within a cylindrical annular duct are presented. In addition, a numerical model for linearized inviscid unsteady flow, which is based upon an existing nonlinear, implicit, wave-split, finite volume analysis, is described. These aerodynamic and numerical models have been implemented into an unsteady flow code, called LINFLUX. A preliminary version of the LINFLUX code is applied herein to selected, benchmark three-dimensional, subsonic, unsteady flows, to illustrate its current capabilities and to uncover existing problems and deficiencies. The numerical results indicate that good progress has been made toward developing a reliable and useful three-dimensional prediction capability. However, some problems, associated with the implementation of an unsteady displacement field and numerical errors near solid boundaries, still exist. Also, accurate far-field conditions must be incorporated into the LINFLUX analysis, so that this analysis can be applied to unsteady flows driven by external aerodynamic excitations.			
14. SUBJECT TERMS Turbomachinery blade rows; Three-dimensional flow; Euler equations; Unsteady perturbations; TURBO nonlinear analysis; LINFLUX linearized analysis; Blade vibration; Aerodynamic excitation; Aeroelastic and aeroacoustic responses		15. NUMBER OF PAGES 36	
17. SECURITY CLASSIFICATION OF REPORT Unclassified		18. SECURITY CLASSIFICATION OF THIS PAGE Unclassified	
19. SECURITY CLASSIFICATION OF ABSTRACT Unclassified		20. LIMITATION OF ABSTRACT A03	





**National Aeronautics and  
Space Administration**

**Lewis Research Center**  
21000 Brookpark Rd.  
Cleveland, OH 44135-3191

Official Business  
Penalty for Private Use \$300

**POSTMASTER: If Undeliverable — Do Not Return**